JCTC Journal of Chemical Theory and Computation

pubs.acs.org/JCTC Article

Transfer Learning Meets Embedded Correlated Wavefunction Theory for Chemically Accurate Molecular Simulations: Application to Calcium Carbonate Ion Pairing

Xuezhi Bian* and Emily A. Carter*

Cite This: J. Chem. Theory Comput. 2026, 22, 5174−5184 Read Online

ABSTRACT: Achieving chemical accuracy for molecular simulations remains a central challenge in computational chemistry. Here, we present an embedded correlated wavefunction transfer learning (ECW-TL) framework for accurately simulating molecular dynamics in the condensed phase. ECW-TL incorporates high-level electron exchange and correlation effects in ECW theory while preserving the training and computational efficiency of machine-learned interatomic potentials. We demonstrate the framework on $Ca^{2+}-CO_3^{2-}$ ion pairing in aqueous solution, a key process underlying CO_2 mineralization in seawater. As proof of principle, we first show that fine-tuning a DFT-revPBE-D3(BJ) baseline model with embedded-DFT-SCAN data reproduces the DFT-SCAN free-energy surface within 1 kcal/mol across all solvation states. Extending the framework to embedded MP2 and localized natural-orbital CCSD(T) further refines the free-energy profile, revealing the crucial role of exact electron exchange and correlation in determining ion-pair stability and structure. The computed ion-pair association free energy is in quantitative agreement with experimental measurements, further validating the accuracy of the ECW-TL framework. ECW-TL thus provides a general, data-efficient route for transferring CW accuracy to efficient simulations of complex aqueous and interfacial chemical processes.

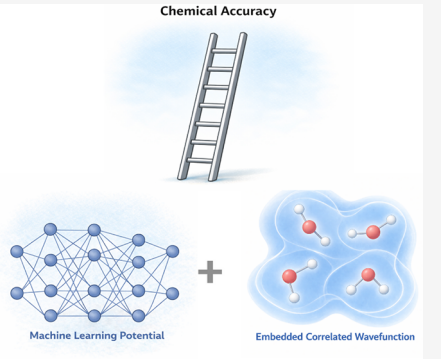

INTRODUCTION

Ab initio molecular dynamics (AIMD) simulation has become a fundamental tool for gaining understanding of microscopic phenomena in molecular and condensed-phase systems,[1,2] providing insights into many processes, including those of interest here, such as solvation[3,4] and proton transfer dynamics.[5,6] Over the past two decades, the development of machine-learned interatomic potentials (MLIPs) has transformed molecular dynamics (MD) simulation further by extending near-first-principles accuracy to larger systems and longer time scales.[7−10] The predictive reliability of both AIMD and MLIP-MD is determined by their underlying electronic structure description, typically provided by density functional theory (DFT).[11,12] However, DFT calculations rely on approximate exchange-correlation (XC) functionals that suffer from self-interaction and delocalization errors,[13] which can lead to quantitative inaccuracy or even complete failure qualitatively.

Correlated wavefunction (CW) theory, in contrast, provides a systematic, physically rigorous route to go beyond DFT and can provide quantitative accuracy.[14] CW methods such as second-order Møller−Plesset perturbation theory (MP2)[15] and coupled-cluster theory with single, double and perturbative triple excitations (CCSD(T))[16] reliably account for electron correlation and exact exchange, enabling a superior description of chemical reaction thermodynamics, especially for main group, closed-shell species.[17,18] That being said, extending CW methods to AIMD or MLIP-MD faces significant challenges.[19−21] First, the computational cost of CW methods increases steeply with system size, rendering their direct application to MD of extended systems intractable. Even with recent advances in local correlation[22,23] and periodic CW algorithms,[24] even static simulations remain limited to systems containing only a few dozen atoms—too small to capture the structural complexity of condensed-phase chemical processes. Second, analytical energy gradients,[25,26] which are essential for MD, are often unavailable or unaffordable for CW methods. The lack of force information further hinders the training of MLIPs, which depend critically on accurate force data to describe high-dimensional energy landscapes.[27]

Many efforts have been made to overcome these challenges. From the electronic structure perspective, a variety of embedding approaches have been developed to enable application of CW theory to extended systems.[28−31] These methods assume that the chemically active region is spatially localized. The local region of interest is then treated with a high-

Received: March 3, 2026
Revised: April 21, 2026
Accepted: April 22, 2026
Published: May 7, 2026

https://doi.org/10.1021/acs.jctc.6c00403
J. Chem. Theory Comput. 2026, 22, 5174−5184

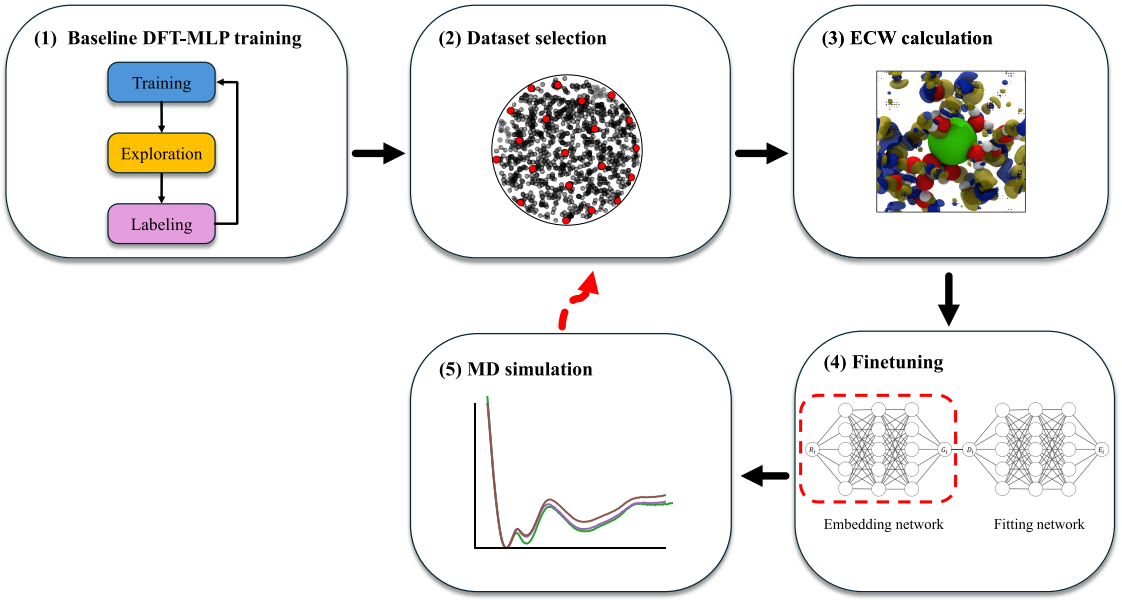

Figure 1. Schematic workflow of the ECW-TL framework. (1) A baseline model is trained using an active-learning workflow. (2) A diverse subset of configurations is selected from the baseline data set. (3) DFET/ECW calculations are performed on the selected configurations. (4) The model is fine-tuned using ECW data, during which part of the neural network (e.g., the embedding network, highlighted by the red dashed circle) is frozen to avoid overfitting. (5) MD simulations are then carried out to assess convergence. If convergence is not achieved, additional data is selected and the fine-tuning cycle is repeated.

level CW theory, while the remaining environment is described using a lower-level DFT method. Among these methods, density functional embedding theory (DFET)[32,33] and the subsequent embedded correlated wavefunction (ECW) theory,[34] which employs the electron density as the embedding variable and a uniquely defined, exact (within DFT) embedding potential to capture reactive-system-environment interactions, offer a balance between computational cost and accuracy. ECW theory has been successfully applied to many systems, including electrocatalysis,[35−40] plasmonic photocatalysis,[41,42] and aqueous-phase reactions.[43−47]

From the machine-learning perspective, transfer learning has emerged as an effective strategy for bridging different levels of electronic-structure theory while greatly reducing the amount of downstream data required.[48−50] Recently, transfer learning has been successfully applied to fine-tune MLIPs for small-molecule data sets[51,52] and liquid water.[53] For example, Chen et al. showed that using as few as 200 data points is sufficient to correct the structural properties of water, demonstrating its capability to systematically refine DFT-based MLIP models toward CW accuracy, even though their periodic CW calculations were limited to small simulation cells (16 waters).[53]

Here, we propose a framework that integrates ECW theory with transfer learning (ECW-TL), combining the efficiency of data-driven transfer-learning approaches with the quantitative accuracy of ECW methods for condensed-phase systems. We demonstrate the capability of ECW-TL by applying it to compute the free-energy profile of calcium−carbonate ion pairing in aqueous solution, a fundamental step in CO_2 mineralization in seawater. Using ECW-TL, we first confirm that transfer learning between two DFT approximations reproduces the target free-energy surface (FES) within chemical accuracy (∼1 kcal/mol) for all critical solvation states and transition states. Then, incorporating embedded periodic MP2 and localized natural-orbital CCSD(T) data further refines the original DFT-revPBE-D3(BJ) FES, yielding a state-of-the-art MLIP that retains ECW-level fidelity. Beyond ion pairing, the ECW-TL framework provides a general, efficient route toward chemically accurate simulations of reactions in complex aqueous and interfacial processes.

ECW-TL FRAMEWORK

As summarized in Figure 1, our ECW-TL framework consists of five stages:

(1) Baseline model training: Train a baseline DFT-MLIP model to accurately reproduce the DFT potential-energy surface and target properties of the system of interest, providing sufficient sampling across relevant configurations. In this work, we use the Deep Potential (DP)[54,55] framework for the MLIP model and an iterative "training—exploration—labeling" active learning procedure to explore and converge the configuration space.[56] During exploration, MLIP-MD samples new configurations using the MLIP from the previous iteration. Each configuration is evaluated by a committee of independently trained MLIPs; those with large force deviations among committee members are flagged as uncertain, labeled to perform reference DFT calculations, and added to the training set for the next iteration.

(2) Representative subset selection: Once the baseline DFT-MLIP model converges, select a representative subset of configurations from the training data set. The selection can be guided by both chemical intuition and structural descriptors that characterize the atomic environments. In this work, we employ a farthest point sampling (FPS) algorithm[57] based on DP local descriptors (of the baseline model) to obtain a diverse subset. The DP local descriptor is defined as the output vector of the embedding network in a DP-MLIP model. For each configuration, we average the local descriptors over all atoms with the same element type to obtain a single configuration-level descriptor used for FPS.

https://doi.org/10.1021/acs.jctc.6c00403
J. Chem. Theory Comput. 2026, 22, 5174−5184

(3) ECW data generation: For each configuration in the selected subset, consistently partition the system into a local region of interest (a "cluster") and its environment. Perform DFET/ECW calculations and collect the ECW-corrected total energies:

$$E_{\mathrm{tot}}^{\mathrm{ECW}} = E_{\mathrm{tot}}^{\mathrm{DFT}} + (E_{\mathrm{emb,cluster}}^{\mathrm{CW}} - E_{\mathrm{emb,cluster}}^{\mathrm{DFT}}) \quad (1)$$

where $E_{\mathrm{emb,cluster}}^{\mathrm{CW}}$ and $E_{\mathrm{emb,cluster}}^{\mathrm{DFT}}$ denote the energies of the embedded cluster computed at the CW and DFT levels of theory in the presence of the embedding potential derived from DFET.

(4) Transfer learning (fine-tuning): Finetune the baseline DFT-MLIP model on the ECW corrected data set. During transfer learning, we empirically freeze early neural network layers (i.e., the embedding network in the DP framework) and use a smaller learning rate to avoid forgetting knowledge of the pretrained DFT-based MLIP model and overfitting to the limited ECW data set.

(5) Validation and iterative refinement: Run MD with the ECW-TL model to evaluate target properties. If the target property does not meet convergence or accuracy criteria, return to stage (2) and select additional configurations for DFET/ECW calculation and continue the iterative cycle until desired accuracy is achieved.

Before moving to our proof-of-principle application, we highlight several key features of the ECW-TL framework. First, no force data is used during fine-tuning, as nuclear gradients remain difficult to compute within ECW theory. The model derives ECW-level forces from energy corrections, effectively reusing and refining the force field learned from the pretrained DFT MLIP model. Second, ECW-TL is trained entirely on condensed-phase configurations, distinguishing it from most of the existing transfer learning or Δ-learning approaches that rely on gas-phase cluster data to extrapolate to bulk systems.[58−63] It is known that such "cluster-to-bulk" training can be problematic due to the distinct structural and electronic environments of isolated clusters versus the condensed phase.[64,65] That said, a similar embedding spirit—albeit classical not quantum—is adopted in a range-corrected Δ-learning approach, where semiempirical quantum mechanical/molecular mechanical (QM/MM) potentials are corrected toward higher-level (e.g., DFT) QM/MM accuracy.[66,67] Third, compared with directly using high-level energies for the training, the ECW-TL framework reduces size and methodological inconsistencies through the ECW energy expression in eq 1. The term in parentheses represents the relative energy difference between two levels of theory, effectively capturing the spirit of Δ-learning within a physically consistent embedding formulation. Together, these features make ECW-TL a practical and general framework for transferring CW accuracy into large-scale molecular simulations.

RESULTS

$Ca^{2+}-CO_3^{2-}$ ion pairing is a fundamental first step in metal−carbonate nucleation toward CO_2 mineralization.[68−70] Long-standing debates exist regarding whether $CaCO_3$ crystallization follows a classical nucleation pathway or proceeds through prenucleation clusters,[71−73] and obtaining a quantitatively accurate ion-pairing FES has been shown to be crucial[73] for large-scale coarse-grained simulations and understanding the microscopic mechanisms of mineral formation.

Accurately simulating $Ca^{2+}-CO_3^{2-}$ ion pairing is a nontrivial task. This process is governed by a subtle balance of electrostatics, polarization, and solvent rearrangement which requires a high-level electronic structure theory treatment to describe accurately. Moreover, ion association and dissociation are rare events controlled by slow solvent reorganization and collective fluctuations, which make the convergence of the FES particularly challenging. As shown in refs 45,74−76 AIMD and MLIP-MD simulations using different electronic structure methods and enhanced-sampling schemes yield qualitatively different energetic orderings of the various solvation states. To this end, the $Ca^{2+}-CO_3^{2-}$ ion-pairing system provides an ideal benchmark for evaluating the accuracy, transferability, and efficiency of our ECW-TL framework.

Following our group's previous work,[45] all electronic structure calculations and MD simulations used for model training were performed using a periodic supercell containing one Ca^{2+} cation, one CO_3^{2-} anion, and 53 water molecules, corresponding to a ∼1 M ionic concentration. This supercell is sufficiently large to capture the three key ion-pair states: bidentate and monodentate contact ion pairs (CIPs), and solvent-shared ion pairs (SSHIPs). It is not large enough to study solvent-separated ion pairs (SSIPs).

Validation

Following the ECW-TL workflow, we start by training a DFT-MLIP at the revised Perdew−Burke−Ernzerhof[77,78] level of theory combined with Grimme's D3 dispersion correction with Becke-Johnson damping[79−81] (revPBE-D3(BJ)) as our baseline model. After 15 active-learning iterations, approximately 7,000 structures were collected to achieve convergence of the baseline DFT-revPBE-D3(BJ) potential. In parallel, we trained another DFT-MLIP using the strongly constrained and appropriately normed (SCAN)[82] functional to serve as our first "high-level" reference.

Enhanced-sampling MLIP-MD simulations were then performed for both models to compute the ion-pairing FES. All simulations were carried out in the NVT ensemble at 330 K, using the Ca−C distance as the only collective variable (CV) with the on-the-fly probability enhanced sampling (OPES) method.[83] The choice of an elevated temperature reflects the upward shift in the melting temperature of water predicted by these DFT functionals.[84,85] As it happens, as shown in Figure S4 in the (Supporting Information SI), the FES is insensitive to temperature in the range of 300−330 K anyway. Previous work[76] established that a single CV is sufficient to capture the ion-pairing mechanism for this system. Further details on the DFT calculations, MLIP training, and enhanced-sampling MD simulations are provided in the Methods section below.

Next, at each ECW/embedded-DFT-SCAN-TL iteration, we selected a subset of configurations from the DFT-revPBE-D3(BJ) MLIP model training set. For each selected configuration in the full periodic cell (e.g., Figure 2a), the cluster of interest was consistently defined as the Ca^{2+} and CO_3^{2-} ions together with their first solvation shell, comprising 14 water molecules as illustrated in Figure 2b,c. This cluster size was validated in our group's earlier work.[45] Then, embedding potentials were generated using DFET (Figure 2d) and embedded-DFT-SCAN calculations were performed to obtain the embedded energy corrections for the cluster in the presence of its environment for these configurations. The resulting embedded-DFT-SCAN energies were used to fine-tune the baseline DFT-revPBE-D3(BJ) MLIP model, after which

https://doi.org/10.1021/acs.jctc.6c00403
J. Chem. Theory Comput. 2026, 22, 5174−5184

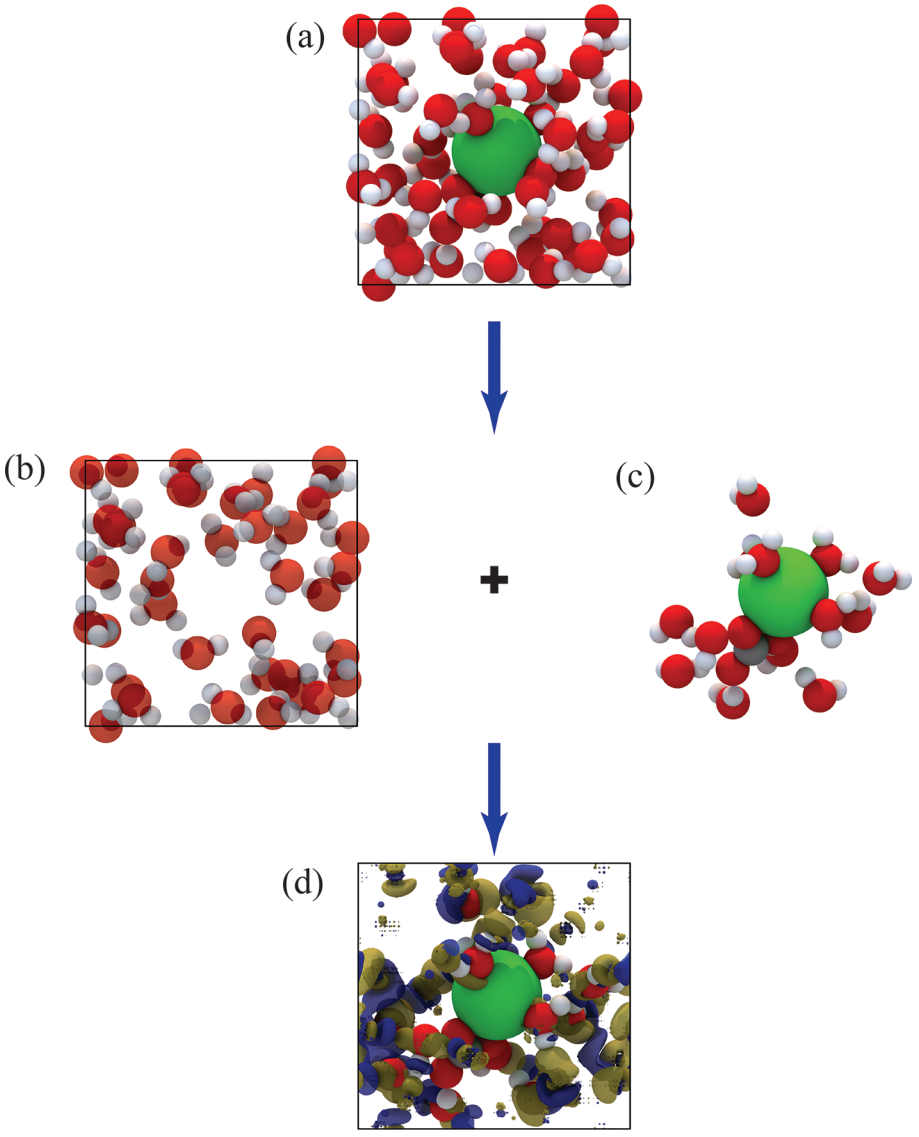

Figure 2. Schematic illustration of the DFET/ECW calculation setup. The total simulation cell (a) is partitioned into a cluster of interest (c) and its surrounding environment (b). The CW calculation is performed on the cluster in the presence of the embedding potential (d) derived from DFET. The blue and yellow isosurfaces represent the attractive and repulsive components of the embedding potential, respectively, plotted at $V_{emb} = \pm 0.3$ V, depicting the interaction between the environment (b) and the cluster (c).

enhanced-sampling MD simulations were carried out to compute the FES with the fine-tuned embedded-DFT-SCAN MLIP model.

In Figure 3a, we show the distribution of fine-tuning data used in each iteration, and in Figure 3b we compare the resulting FESs obtained from the two DFT-based models (revPBE-D3(BJ) and SCAN) and the embedded-DFT-SCAN fine-tuned models at successive ECW-TL iterations. Comparing the two DFT models, we find the DFT-revPBE-D3(BJ) baseline model qualitatively disagrees with the DFT-SCAN model; in particular, DFT-revPBE-D3(BJ) model predicts the monodentate state to be more stable than the bidentate state. This discrepancy again highlights the need to go beyond functional-dependent DFT models to obtain a quantitatively reliable description. For further context, a comparison with previously reported DFT-revPBE-D3(BJ) and DFT-SCAN-derived FESs is shown in Figure S9 of the SI, with an accompanying discussion.

We next turn to the transfer learning results. In the first iteration, approximately 700 configurations from the training data set of the baseline DFT-revPBE-D3(BJ) model were uniformly selected along the Ca−C distance using the FPS algorithm. After the first fine-tuning iteration, the FES predicted by the embedded-DFT-SCAN model clearly shifts from the baseline DFT-revPBE-D3(BJ) result toward the reference DFT-SCAN result and correctly recovers the free energy ordering. However, deviations remain in the transition regions between the bidentate ($R_{Ca-C} \approx 2.8$ Å) and monodentate ($R_{Ca-C} \approx 3.3$ Å) CIP states, as well as between the monodentate CIP and the SSHIP ($R_{Ca-C} \approx 4.8$ Å) states. To further improve accuracy, an additional 400 original baseline model configurations from the bidentate−monodentate region were incorporated in iteration 2, which significantly refined the FES in that region. In iteration 3, another 400 original baseline model configurations were added from the monodentate-SSHIP region, further improving agreement with the DFT-SCAN reference. The additional data in iterations 2 and 3 were also selected using the FPS algorithm. Note that because only embedded-DFT-SCAN energies are used for fine-tuning here, force-deviation-based active learning is

https://doi.org/10.1021/acs.jctc.6c00403
J. Chem. Theory Comput. 2026, 22, 5174−5184

not very effective during fine-tuning, as the limited size of the energy-only high-level data set leads to small diversity among committee models and nearly identical force predictions.

With this fine-tuning data set of ∼1,500 configurations, we find the embedded-DFT-SCAN model successfully reproduces the reference DFT-SCAN FES across all critical solvation states and transition states with an accuracy better than 1 kcal/mol. These results demonstrate that the selected data set effectively samples the relevant configuration space and that the ECW-TL framework therefore should reliably transfer from DFT to high-level ECW theory with a reasonable amount of data. Note that all fine-tuning configurations (iterations 1−3) are selected from the training data set of the baseline model. Therefore, the improvement must arise from transfer learning to higher-level theory rather than the introduction of new configurations. Finally, for comparison we performed transfer learning using the vacuum-cluster-corrected energies (see Section S5 in the SI for more details) while keeping the training configurations and procedure fixed. Our ECW-TL approach is significantly more accurate than the vacuum-cluster transfer learning, highlighting the importance of using the embedding formalism. The results are shown in Figure S8 of the SI.

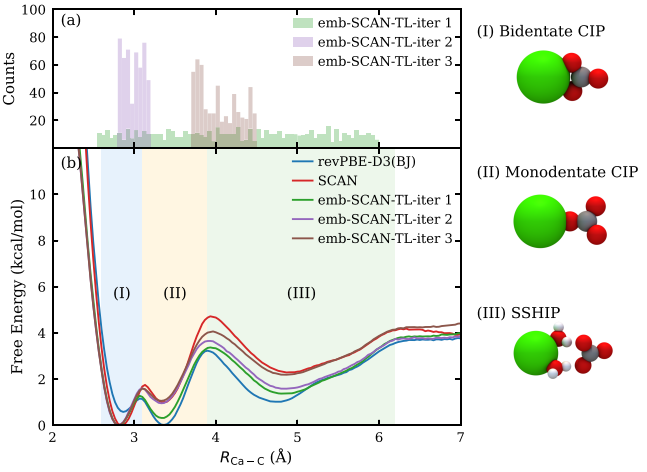

Figure 3. (a) Distribution of the fine-tuning data set along the Ca−C distance used in each ECW-TL iteration. (b) Free-energy surfaces computed from the two DFT models and the embedded-DFT-SCAN fine-tuned models at successive iterations. Distinct ion-pair state regions (I), (II) and (III) are highlighted by different colors, with representative schematic structures shown on the right (Ca in green, C gray, O red, H white). The embedded-DFT-SCAN model systematically improves throughout the ECW-TL workflow and achieves near-reference accuracy by iteration 3 across all critical ion-pair states.

Application

Building on the success of the DFT-level fine-tuning, we applied the ECW-TL framework to incorporate higher-level ECW methods. To avoid spurious cluster-image interactions arising from the finite supercell, we employed periodic Gaussian-type orbital (GTO) embedded DFT and ECW calculations, ensuring a consistent treatment of interactions between the cluster, the periodic environment, and all periodic replicas. Note that the embedded-DFT-revPBE-D3(BJ) and embedded-DFT-SCAN energies used for fine-tuning in the Validation section above also were computed within the periodic GTO formalism. This periodic approach is somewhat different from previous DFET/ECW calculations, as detailed further in the Methods section below and the SI.

Using the same structural data set combined from the three fine-tuning iterations above (containing all ∼1500 configurations), we performed periodic embedded MP2 and periodic embedded localized natural orbital CCSD(T) (LNOCCSD(T))[86] calculations and fine-tuned the DFT-revPBE-D3 (BJ) baseline model accordingly. The resulting ECW-TL-MP2 and ECW-TL-LNOCCSD(T) free-energy surfaces are shown in Figure 4. Remarkably, the ECW-TL-

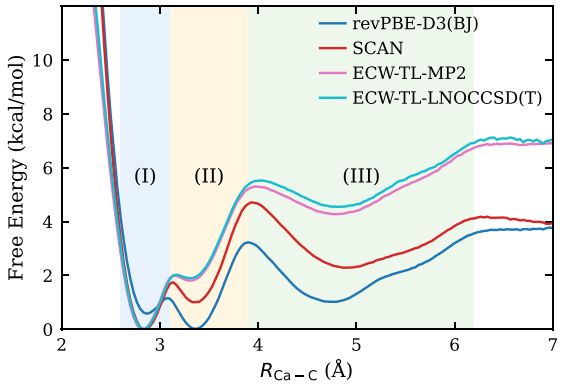

Figure 4. Free-energy surfaces computed from the two DFT-level models and the two ECW-TL fine-tuned models. The two ECW-TL models agree with each other but differ qualitatively from both DFT models. See definitions of ion-pairing regions I−III in the caption of Figure 3.

MP2 and ECW-TL-LNOCCSD(T) results are in excellent agreement with each other, consistent with previous findings[45] that MP2 provides near-quantitative accuracy for this system. Notably, DFT-revPBE-D3(BJ) fails to capture the enhanced stability of the bidentate configuration relative to the monodentate state, whereas DFT-SCAN, MP2, and LNOCCSD(T) consistently predict this ordering, providing strong evidence that this reflects the physically correct description. However, although the overall energetic ordering agrees with DFT-SCAN model, both ECW-TL-MP2 and ECW-TL-LNOCCSD(T) predict a significantly larger free-energy difference (∼5 kcal/mol) between the SSHIP and bidentate states compared to either DFT model (∼1−2 kcal/mol), showing how CW methods substantially modify the relative stability of the ion-pairing states.

The reduction of the SSHIP to CIP barrier from ∼2 kcal/mol predicted by the semilocal DFT models to ∼1 kcal/mol obtained from ECW models highlights the impact of DFT delocalization error, which spuriously stabilizes charge-separated states like the SSHIP and hence overestimates the free-energy barrier for CIP formation.[75] In contrast, models based on ECW theory eliminate this artifact[45,46] and thus provide a more quantitatively accurate description of the ion-pairing energetics.

Although the free energy profiles cannot be compared directly with experiment, one important quantity that can be compared is the ion-pair association free energy ΔG. According to ref 88, this quantity can be calculated as

$$\Delta G = -k_B T \ln c_0 \int_0^{r_c} dr 4\pi r^2 e^{-\frac{W(r)}{k_B T}} \quad (2)$$

Here, $W(r) = F(r) - k_B T \ln 4\pi r^2$ is the free energy profile with the geometric entropy contribution (the second term) removed,

https://doi.org/10.1021/acs.jctc.6c00403
J. Chem. Theory Comput. 2026, 22, 5174−5184

where r is the ion-separation distance (R_{Ca-C}), and c_0 is the concentration of 1 M. Note that $W(r)$ is equated at the integral cutoff distance r_c to the electrostatic interaction $E(r) = -\frac{qQ}{4\pi\epsilon_r\epsilon_0 r}$, where q and Q are the charges of Ca^{2+} and CO_3^{2-} ions, ϵ_0 is the vacuum permittivity and ϵ_r is the dielectric constant of water, which we take to be 78. The ion-pair association free energy predicted by different models are shown in Figure 5 and

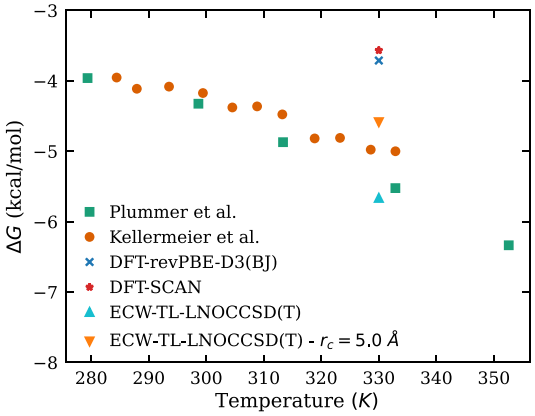

Figure 5. Comparison between experimental[69,87] and simulated ion-pair association free energies ΔG. Unless otherwise noted, simulation values are computed using r_c = 6 Å. Results from DFT-based models and the ECW-TL-LNOCCSD(T) model are shown, with the latter exhibiting improved agreement with experiment. For ECW-TL-LNOCCSD(T), results obtained with r_c = 5 Å are also included to indicate the uncertainty associated with the cutoff choice and finite size effects.

compared with experimental results reported by Plummer et al.[87] and Kellermeier et al.[69] Here, we choose r_c = 6 Å which corresponds to approximately half the simulation cell length.

At the simulation temperature of 330 K, both DFT-based models predict ion-pair association free energies of about −3.6 kcal/mol, whereas the experimental value lies in the range of −5.6 to −4.9 kcal/mol. In contrast, the ECW-TL-LNOCCSD(T) model predicts a value of −5.7 kcal/mol. Note that two main factors may introduce uncertainty into this calculation. First, the result depends on the choice of the cutoff distance r_c. Because our simulation does not fully sample the SSIP region due to finite size effects, using a cutoff of 6 Å may lead to an overestimation of the association free energy. To assess this effect, we also report results using r_c = 5 Å where the alignment point lies within the SSIP region basin. This choice provides an upper bound, as shown in Figure 5, and we find that the experimental values fall well within the resulting range. Second, the current MLIP models are short-ranged and may miss long-range electrostatic interactions. Incorporating long-range effects within the ECW-TL framework is an important direction for future work. Nevertheless, the ECW-TL-LNOCCSD(T) model predicts the ion-pair association free energy within chemical accuracy, demonstrating its predictive power for condensed-phase interactions.

Next, we turn to the structural properties obtained from the four models discussed above. We performed constrained MD simulations at the bidentate CIP, monodentate CIP, and SSHIP minima, holding the Ca−C distance fixed at each minimum while allowing all other degrees of freedom to be dynamically sampled. As shown in Figure 6, in all three cases, the embedded-DFT-SCAN model accurately reproduces the Ca−O_w (cal-

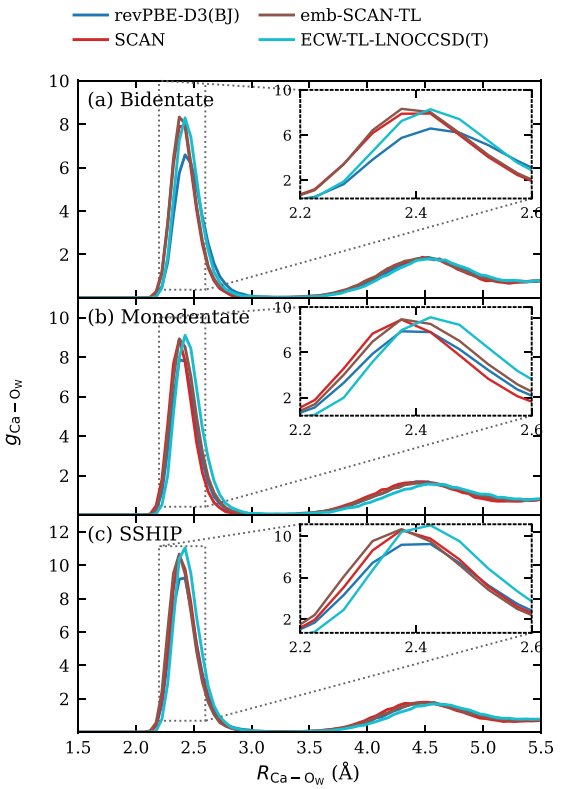

Figure 6. Ca−O_w RDFs computed from the four models at three representative Ca−C distances: (a) Bidentate CIP minimum (R_{Ca-C} = 2.8 Å)), (b) monodentate CIP minimum (R_{Ca-C} = 3.3 Å) and (c) SSHIP minimum (R_{Ca-C} = 4.8 Å). The fine-tuned emb-DFT-SCAN model agrees nearly perfectly with the full DFT-SCAN model, which is remarkable, given that no forces (only energies) from emb-DFT-SCAN were used in the fine-tuning. The first solvation shell structure ($R_{Ca-O_W} \approx 2.4$ Å) predicted by both fine-tuned models differs qualitatively from the baseline DFT-revPBE-D3(BJ) model.

cium−water oxygen) radial distribution function (RDF) compared to the DFT-SCAN reference and exhibits noticeable deviations from the baseline DFT-revPBE-D3(BJ) model. This demonstrates that our ECW-TL framework can capture not only the relative energetics but also the potential-energy landscape and the equilibrium structural distributions of the target high-level theory. Furthermore, DFT-SCAN, embedded DFT-SCAN fine-tuned and ECW-TL-LNOCCSD(T) models have a larger peak at the first solvation shell of Ca^{2+} ($R_{Ca-O_W} \approx 2.4$ Å) compared to the DFT-revPBE-D3(BJ) model (insets of Figure 6), indicating a more tightly coordinated first hydration shell. This difference reflects the improved treatment of exchange and correlation in the SCAN and CW-based descriptions (more localized cation charge due to less delocalization error), which modifies the short-range, ion−water interaction potential.

In Figure 7, we further analyze the global structural properties through the oxygen−oxygen RDF of the water molecules. Notably, all fine-tuned models reproduce the water structure of the baseline model rather than that of the higher-level references. This behavior is expected, as ECW corrections are applied only within the localized embedded cluster and do not affect the environmental water dynamics. Nevertheless, this level of accuracy is sufficient for our purposes, as most chemical processes involve local chemical bond changes, which the ECW-TL framework is designed to capture effectively, as shown by the ion-pairing FES.

https://doi.org/10.1021/acs.jctc.6c00403
J. Chem. Theory Comput. 2026, 22, 5174−5184

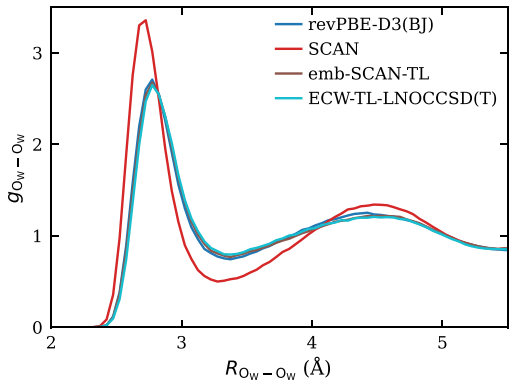

Figure 7. O_w−O_w RDFs computed from the four models. Neither the embedded-DFT-SCAN fine-tuned model nor the ECW-TL-LNOCCSD(T) model alters the bulk water structure relative to the baseline DFT-revPBE-D3(BJ) models, as expected.

DISCUSSION AND CONCLUSIONS

While these results validate the overall reliability of our ECW-TL framework, certain limitations remain. In Figure 3b, at the transition state between the monodentate CIP and SSHIP regions (R_{Ca-C} = 4.0 Å), a ∼0.6 kcal/mol discrepancy exists between the third iteration embedded-DFT-SCAN and the reference DFT-SCAN results. We attempted to reduce this error by adding more configurations to the fine-tuning data set but the results exhibited convergence behavior close to iteration 3, indicating that the remaining difference is likely not due to insufficient training data. This small residual error may arise from multiple sources. One possible interpretation is that, along the pathway from the SSHIP to the monodentate CIP structure, a water molecule may leave the first solvation shell and diffuse into the bulk solvent, which is not accounted for within the DFET/ECW partitioning definition. Figure 8 displays the 2D FES from the underlying DFT-revPBE-D3(BJ) theory (see Methods for details), in which both five- and six-fold coordination states are seen to be equally accessible and readily interchangeable in the CIP basin, whereas the SSHIP basin is predominantly six-fold coordinated (based on the deeper blue color of the well). This suggests that CIP formation can be coupled to the release of a water molecule from the first solvation shell, among various paths for CIP formation. Accurately learning this process requires high-level information about the extended water interactions, which is difficult to include with the current embedded cluster size. Another possibility is the limited representation ability of the current MLIP model architecture. In the future, it will be valuable to explore the influence of the embedded cluster size and to test more advanced MLIP architectures, for example, multihead architectures trained simultaneously on multiple levels of theory, or message-passing models that better capture many-body correlations.

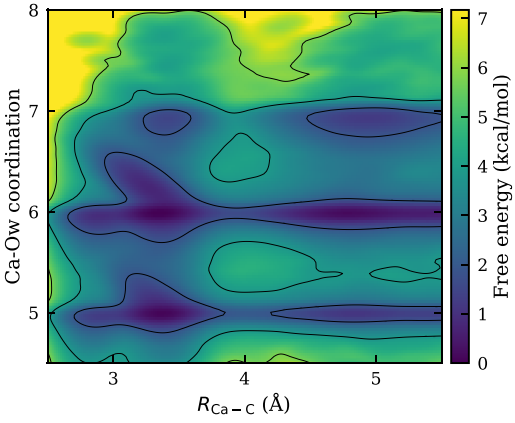

Figure 8. Two-dimensional free-energy surface as a function of the Ca−C distance and Ca−O_w coordination number, computed from the DFT-revPBE-D3(BJ) MLIP model with the Ca−C distance as the only enhanced sampling CV. Along the pathway from the SSHIP minimum to the monodentate CIP minimum, the Ca^{2+} ion can adopt either five- or six-fold coordination with water molecules.

Moreover, as discussed above, the present ECW-TL framework focuses primarily on local dynamics and is thus less suited for capturing statistical observables in homogeneous systems. A potential path forward we are currently exploring is a divide-and-conquer strategy, in which a large simulation cell is partitioned into multiple clusters and ECW calculations can be performed on each cluster.

Finally, note that the ECW methods used here—embedded MP2 and CCSD(T)—are not well suited for electrochemical systems involving metals, and multireference approaches such as complete active space self-consistent field (CASSCF) and beyond are required. In such cases, one must ensure not only a consistent choice of embedded cluster size but also a consistent active space across different configurations,[89] aspects that we plan to address in future ECW-TL work.

In summary, the ECW-TL framework provides a practical route for transferring CW accuracy to MLIPs in the condensed phase. By combining high-level ECW corrections with systematic fine-tuning of DFT-MLIPs, we achieve a quantitative description of ion-pairing thermodynamics that is inaccessible to standard DFT models. The FES obtained from the "gold-standard" embedded LNO−CCSD(T) calculations should approach nearly chemical accuracy for condensed-phase systems containing only closed-shell main group molecules. Future extensions incorporating multiple ion pairs and larger ionic clusters into the training set, combined with coarse-grained modeling strategies, will enable access to larger length and time scales more relevant to nucleation phenomena.[73] Given its generality, the ECW-TL approach holds great promise for direct application to a broad range of condensed-phase reactions beyond ion pairing, combining the accuracy of ECW with long-time, large-scale sampling of MLIPs.

METHODS

DFT

Periodic plane-wave DFT calculations were performed using the all-electron, frozen-core, projector augmented-wave (PAW) method within the Vienna Ab initio Simulation Package (VASP).[90,91] The standard PBE PAW potentials were employed for O, C, and H, and the PBE PAW potential with 3s and 3p semicore states treated as valence states was used for Ca. A kinetic-energy cutoff of 720 eV was applied, and all calculations were carried out using Γ-point k-point sampling. Gaussian smearing with a width of 0.1 eV was used to accelerate convergence, with the DFT convergence threshold set to 10^{-6} eV. All configurations consisted of 53 water molecules and one Ca-CO_3 ion pair within an orthorhombic simulation cell of dimensions 12.28 Å × 11.82 Å × 11.55 Å.

DFET/ECW

Embedding potentials $V_{emb}(\boldsymbol{r})$ on real space grids within the periodic cell were generated at the DFT-revPBE-D3(BJ) level in a modified version of VASP[92] via PAW-DFET within a planewave basis by maximizing an extended Wu−Yang functional:[93,94]

https://doi.org/10.1021/acs.jctc.6c00403
J. Chem. Theory Comput. 2026, 22, 5174−5184

$$W = E^{\mathrm{DFT}}_{\mathrm{cluster}}[\rho_{\mathrm{cluster}},\ V_{\mathrm{emb}}] + E^{\mathrm{DFT}}_{\mathrm{enviro}}[\rho_{\mathrm{enviro}},\ V_{\mathrm{emb}}] - \int d\boldsymbol{r} V_{\mathrm{emb}}(\boldsymbol{r})\rho_{\mathrm{tot}}(r) \quad (3)$$

where: $E^{\mathrm{DFT}}_{\mathrm{cluster}}$ and $E^{\mathrm{DFT}}_{\mathrm{enviro}}$ are self-consistent DFT energies of the cluster and its environment subject to the added external potential, V_{emb}; ρ_{cluster} and ρ_{enviro} represent the corresponding electron densities; and convergence is reached within the DFET when the total electron density from the entire periodic cell $\rho_{\mathrm{tot}} = \rho_{\mathrm{cluster}} + \rho_{\mathrm{enviro}}$. For additional details, we refer the reader to refs 33,41, and 87.

The embedding potentials on the real-space grid then were projected onto a cc-pVTZ[95] basis set for use in our periodic embedded calculations.[96] Embedded periodic GTO DFT-revPBE-D3(BJ), DFT-SCAN and ECW calculations then were performed using the PySCF package.[97] Embedded periodic planewave DFT and embedded periodic GTO DFT total energies agree quite well with each other (Figure S6), validating our choice to perform embedded periodic GTO calculations for both parts of the regional correction term in eq 1 for basis set consistency, and thereby capturing both periodic image interactions and enabling periodic CW calculations in the regional correction term. The periodic LNOCCSD(T) calculations were performed using a separate branch of PySCF.[98] The final LNO−CCSD(T) energies were augmented with a ΔMP2 correction for improved convergence, following the procedure described in ref 86. For more computational details and convergence tests (Figures S5 and S7) on periodic GTO calculations, see the SI.

MLIP

MLIPs were trained using the DeePMD-kit package[99] together with an active-learning procedure implemented in the DPGEN package.[56] All models used the standard short-range, smooth two-body descriptor with a cutoff radius of r_c = 6 Å. We used the "finetune" function in DeePMD-kit for transfer learning and froze the embedding network during fine-tuning. For additional details on the training procedure, validation (Figures S1 and S2), fine-tuning protocol, and assessment of the MLIP models, see the SI.

MD

The FESs shown in the main text were computed using the OPES method with a metadynamics-like target distribution[83] implemented in the LAMMPS package[100] with the PLUMED plugin.[101] Each FES was obtained by averaging four FESs calculated from four independent 20 ns trajectories to ensure sufficient sampling. The Ca-Ow coordination number was defined according to a cubic switching function[101] with $D_{\max}$ = 3.75 Å and D_0 = 2.5 Å. More details are provided in the SI, where we also compare results with the constrained reaction coordinate, blue-moon ensemble (BME) MD method;[102,103] the two methods exhibit excellent agreement with each other (Figure S3).

■ ASSOCIATED CONTENT

Data Availability Statement

The training data, ML models, and all input scripts to reproduce the simulations are available at https://doi.org/10.34770/3eh9-qm63.

Supporting Information

The Supporting Information is available free of charge at https://pubs.acs.org/doi/10.1021/acs.jctc.6c00403.

> Details and validation of machine-learned interatomic potentials; comparison of enhanced sampling methods; temperature effects; details and convergence tests for periodic ECW calculations; comparison between ECW-TL and direct cluster Δ-learning; comparison of DFT-based FESs with related previous studies (PDF)

■ AUTHOR INFORMATION

Corresponding Authors

Emily A. Carter − *Department of Mechanical and Aerospace Engineering, Princeton University, Princeton, New Jersey 08544, United States; Andlinger Center for Energy and the Environment and Program in Applied and Computational Mathematics, Princeton University, Princeton, New Jersey 08544, United States;* orcid.org/0000-0001-7330-7554; Email: eac@princeton.edu

Xuezhi Bian − *Department of Chemistry, Princeton University, Princeton, New Jersey 08544, United States;* orcid.org/0000-0001-6445-7462; Email: xzbian@princeton.edu

Complete contact information is available at: https://pubs.acs.org/10.1021/acs.jctc.6c00403

Notes

The authors declare no competing financial interest.

■ ACKNOWLEDGMENTS

This work was supported by the Computational Chemical Science Center: Chemistry in Solution and at Interfaces, supported as part of the Computational Chemical Sciences Program funded by the U.S. Department of Energy (DOE), Office of Science, Basic Energy Sciences, under Award No. DESC0019394. X.B. was also partially supported by the BP Carbon Mitigation Initiative (CMI) and the Princeton Catalysis Initiative at Princeton University. We acknowledge the computational resources provided by the National Energy Research Scientific Computing Center (NERSC), which is supported by the DOE Office of Science under Contract No. DE-AC0205CH11231, and Princeton Research Computing at Princeton University. X.B. thanks Pablo Piaggi, Hong-zhou Ye, Lingqing Peng, Ziyang Wei, and John Mark Martirez for helpful discussions.

■ REFERENCES

(1) Car, R.; Parrinello, M. Unified Approach for Molecular Dynamics and Density-Functional Theory. *Phys. Rev. Lett.* **1985**, *55* (22), 2471−2474.

(2) Marx, D.; Hutter, J. *Ab Initio Molecular Dynamics: Basic Theory and Advanced Methods*; Cambridge University Press, 2009.

(3) Tuckerman, M.; Laasonen, K.; Sprik, M.; Parrinello, M. Ab Initio Molecular Dynamics Simulation of the Solvation and Transport of Hydronium and Hydroxyl Ions in Water. *J. Chem. Phys.* **1995**, *103* (1), 150−161.

(4) Ramaniah, L. M.; Bernasconi, M.; Parrinello, M. Ab Initio Molecular-Dynamics Simulation of K+ Solvation in Water. *J. Chem. Phys.* **1999**, *111* (4), 1587−1591.

(5) Geissler, P. L.; Dellago, C.; Chandler, D.; Hutter, J.; Parrinello, M. Ab Initio Analysis of Proton Transfer Dynamics in (H2O)3H+. *Chem. Phys. Lett.* **2000**, *321* (3), 225−230.

(6) Marx, D. Proton Transfer 200 Years after von Grotthuss: Insights from Ab Initio Simulations. *Chemphyschem Eur. J. Chem. Phys. Phys. Chem.* **2006**, *7* (9), 1848−1870.

(7) Behler, J.; Parrinello, M. Generalized Neural-Network Representation of High-Dimensional Potential-Energy Surfaces. *Phys. Rev. Lett.* **2007**, *98* (14), 146401.

(8) Behler, J. Perspective: Machine Learning Potentials for Atomistic Simulations. *J. Chem. Phys.* **2016**, *145* (17), 170901.

(9) Noé, F.; Tkatchenko, A.; Müller, K.-R.; Clementi, C. Machine Learning for Molecular Simulation. *Annu. Rev. Phys. Chem.* **2020**, *71*, 361−390.

(10) Unke, O. T.; Chmiela, S.; Sauceda, H. E.; Gastegger, M.; Poltavsky, I.; Schütt, K. T.; Tkatchenko, A.; Müller, K.-R. Machine Learning Force Fields. *Chem. Rev.* **2021**, *121* (16), 10142−10186.
(11) Hohenberg, P.; Kohn, W. Inhomogeneous Electron Gas. *Phys. Rev.* **1964**, *136* (3B), B864−B871.
(12) Kohn, W.; Sham, L. J. Self-Consistent Equations Including Exchange and Correlation Effects. *Phys. Rev.* **1965**, *140* (4A), A1133−A1138.
(13) Cohen, A. J.; Mori-Sánchez, P.; Yang, W. Insights into Current Limitations of Density Functional Theory. *Science* **2008**, *321* (5890), 792−794.
(14) Helgaker, T.; Jorgensen, P.; Olsen, J. *Molecular Electronic-Structure Theory*; John Wiley & Sons, 2013.
(15) Møller, C.; Plesset, M. S. Note on an Approximation Treatment for Many-Electron Systems. *Phys. Rev.* **1934**, *46* (7), 618−622.
(16) Raghavachari, K.; Trucks, G. W.; Pople, J. A.; Head-Gordon, M. A Fifth-Order Perturbation Comparison of Electron Correlation Theories. *Chem. Phys. Lett.* **1989**, *157* (6), 479−483.
(17) Stanton, J. F. Why CCSD(T) Works: A Different Perspective. *Chem. Phys. Lett.* **1997**, *281* (1), 130−134.
(18) Fink, R. F. Why Does MP2 Work? *J. Chem. Phys.* **2016**, *145* (18), 184101.
(19) da Silva, A. J. R.; Cheng, H.-Y.; Gibson, D. A.; Sorge, K. L.; Liu, Z.; Carter, E. A. Limitations of Ab Initio Molecular Dynamics Simulations of Simple Reactions: F + H2 as a Prototype. *Spectrochim. Acta, Part A* **1997**, *53* (8), 1285−1299.
(20) Hayes, R. L.; Fattal, E.; Govind, N.; Carter, E. A. Long Live Vinylidene! A New View of the H2CC: → HC⋮CH Rearrangement from Ab Initio Molecular Dynamics. *J. Am. Chem. Soc.* **2001**, *123* (4), 641−657.
(21) Nandi, A.; Qu, C.; Houston, P. L.; Conte, R.; Bowman, J. M. Δ-Machine Learning for Potential Energy Surfaces: A PIP Approach to Bring a DFT-Based PES to CCSD(T) Level of Theory. *J. Chem. Phys.* **2021**, *154* (5), 051102.
(22) Rolik, Z.; Szegedy, L.; Ladjánszki, I.; Ladóczki, B.; Kállay, M. An Efficient Linear-Scaling CCSD(T) Method Based on Local Natural Orbitals. *J. Chem. Phys.* **2013**, *139* (9), 094105.
(23) Guo, Y.; Riplinger, C.; Becker, U.; Liakos, D. G.; Minenkov, Y.; Cavallo, L.; Neese, F. Communication: An Improved Linear Scaling Perturbative Triples Correction for the Domain Based Local Pair-Natural Orbital Based Singles and Doubles Coupled Cluster Method [DLPNO-CCSD(T)]. *J. Chem. Phys.* **2018**, *148* (1), 011101.
(24) Booth, G. H.; Tsatsoulis, T.; Chan, G. K.-L.; Grüneis, A. From Plane Waves to Local Gaussians for the Simulation of Correlated Periodic Systems. *J. Chem. Phys.* **2016**, *145* (8), 084111.
(25) Pople, J. A.; Krishnan, R.; Schlegel, H. B.; Binkley, J. S. Derivative Studies in Hartree-Fock and Møller-Plesset Theories. *Int. J. Quantum Chem.* **1979**, *16* (S13), 225−241.
(26) Harding, M. E.; Metzroth, T.; Gauss, J.; Auer, A. A. Parallel Calculation of CCSD and CCSD(T) Analytic First and Second Derivatives. *J. Chem. Theory Comput.* **2008**, *4* (1), 64−74.
(27) Tokita, A. M.; Behler, J. How to Train a Neural Network Potential. *J. Chem. Phys.* **2023**, *159* (12), 121501.
(28) Huang, P.; Carter, E. A. Advances in Correlated Electronic Structure Methods for Solids, Surfaces, and Nanostructures. *Annu. Rev. Phys. Chem.* **2008**, *59*, 261−290.
(29) Chung, L. W.; Sameera, W. M. C.; Ramozzi, R.; Page, A. J.; Hatanaka, M.; Petrova, G. P.; Harris, T. V.; Li, X.; Ke, Z.; Liu, F.; Li, H.-B.; Ding, L.; Morokuma, K. The ONIOM Method and Its Applications. *Chem. Rev.* **2015**, *115* (12), 5678−5796.
(30) Sun, Q.; Chan, G. K.-L. Quantum Embedding Theories. *Acc. Chem. Res.* **2016**, *49* (12), 2705−2712.
(31) Yu, K.; Krauter, C. M.; Dieterich, J. M.; Carter, E. A. Density and Potential Functional Embedding: Theory and Practice, In *Fragmentation: Toward Accurate Calculations on Complex Molecular Systems*, Gordon, M. S., Ed.. John Wiley & Sons, Ltd, 2017; pp. 81−117. .
(32) Govind, N.; Wang, Y. A.; da Silva, A. J. R.; Carter, E. A. Accurate Ab Initio Energetics of Extended Systems via Explicit Correlation Embedded in a Density Functional Environment. *Chem. Phys. Lett.* **1998**, *295* (1), 129−134.
(33) Huang, C.; Pavone, M.; Carter, E. A. Quantum Mechanical Embedding Theory Based on a Unique Embedding Potential. *J. Chem. Phys.* **2011**, *134* (15), 154110.
(34) Libisch, F.; Huang, C.; Carter, E. A. Embedded Correlated Wavefunction Schemes: Theory and Applications. *Acc. Chem. Res.* **2014**, *47* (9), 2768−2775.
(35) Zhao, Q.; Martirez, J. M. P.; Carter, E. A. Revisiting Understanding of Electrochemical CO2 Reduction on Cu(111): Competing Proton-Coupled Electron Transfer Reaction Mechanisms Revealed by Embedded Correlated Wavefunction Theory. *J. Am. Chem. Soc.* **2021**, *143* (16), 6152−6164.
(36) Zhao, Q.; Martirez, J. M. P.; Carter, E. A. Charting C−C Coupling Pathways in Electrochemical CO2 Reduction on Cu(111) Using Embedded Correlated Wavefunction Theory. *Proc. Natl. Acad. Sci. U. S. A.* **2022**, *119* (44), No. e2202931119.
(37) Zhao, Q.; Martirez, J. M. P.; Carter, E. A. Electrochemical Hydrogenation of CO on Cu(100): Insights from Accurate Multiconfigurational Wavefunction Methods. *J. Phys. Chem. Lett.* **2022**, *13* (44), 10282−10290.
(38) Cai, J.; Zhao, Q.; Hsu, W.-Y.; Choi, C.; Liu, Y.; Martirez, J. M. P.; Chen, C.; Huang, J.; Carter, E. A.; Huang, Y. Highly Selective Electrochemical Reduction of CO2 into Methane on Nanotwinned Cu. *J. Am. Chem. Soc.* **2023**, *145* (16), 9136−9143.
(39) Martirez, J. M. P.; Carter, E. A. C−C Bond Formation during Electrochemical CO2 Reduction on Pristine Cu(100) Unlikely to Involve Adsorbed CO at Any Potential. *J. Am. Chem. Soc.* **2026**, *148* (7), 7415−7425.
(40) Martirez, J. M. P.; Carter, E. A. Insights into Nonelectroactive C−C Bond Formation on Cu(100) during Electrochemical CO2 Reduction from Multiconfigurational Wavefunction Theory. *J. Phys. Chem. C* **2026**, *130*, 3767.
(41) Martirez, J. M. P.; Bao, J. L.; Carter, E. A. First-Principles Insights into Plasmon-Induced Catalysis. *Annu. Rev. Phys. Chem.* **2021**, *72* (1), 99−119.
(42) Wen, X.; Martirez, J. M. P.; Carter, E. A. Plasmon-Driven Ammonia Decomposition on Pd(111): Hole Transfer's Role in Changing Rate-Limiting Steps. *ACS Catal.* **2024**, *14* (12), 9539−9553.
(43) Martirez, J. M. P.; Carter, E. A. Solvent Dynamics Are Critical to Understanding Carbon Dioxide Dissolution and Hydration in Water. *J. Am. Chem. Soc.* **2023**, *145* (23), 12561−12575.
(44) Boyn, J.-N.; Carter, E. A. Probing pH-Dependent Dehydration Dynamics of Mg and Ca Cations in Aqueous Solutions with Multi-Level Quantum Mechanics/Molecular Dynamics Simulations. *J. Am. Chem. Soc.* **2023**, *145* (37), 20462−20472.
(45) Boyn, J.-N.; Carter, E. A. Characterizing the Mechanisms of Ca and Mg Carbonate Ion-Pair Formation with Multi-Level Molecular Dynamics/Quantum Mechanics Simulations. *J. Phys. Chem. B* **2023**, *127* (50), 10824−10832.
(46) Boyn, J.-N.; Carter, E. A. Elucidating and Contrasting the Mechanisms for Mg and Ca Sulfate Ion-Pair Formation with Multi-Level Embedded Quantum Mechanics/Molecular Dynamics Simulations. *J. Chem. Phys.* **2024**, *161* (22), 224501.
(47) Bobell, B.; Boyn, J.-N.; Martirez, J. M. P.; Carter, E. A. Modeling Bicarbonate Formation in an Alkaline Solution with Multi-Level Quantum Mechanics/Molecular Dynamics Simulations. *Mol. Phys.* **2025**, *123* (7−8), No. e2375370.
(48) Zhang, D.; Liu, X.; Zhang, X.; Zhang, C.; Cai, C.; Bi, H.; Du, Y.; Qin, X.; Peng, A.; Huang, J.; Li, B.; Shan, Y.; Zeng, J.; Zhang, Y.; Liu, S.; Li, Y.; Chang, J.; Wang, X.; Zhou, S.; Liu, J.; Luo, X.; Wang, Z.; Jiang, W.; Wu, J.; Yang, Y.; Yang, J.; Yang, M.; Gong, F.-Q.; Zhang, L.; Shi, M.; Dai, F.-Z.; York, D. M.; Liu, S.; Zhu, T.; Zhong, Z.; Lv, J.; Cheng, J.; Jia, W.; Chen, M.; Ke, G.; E, W.; Zhang, L.; Wang, H. DPA-2: A Large Atomic Model as a Multi-Task Learner. *Npj Comput. Mater.* **2024**, *10* (1), 293.
(49) Niblett, S. P.; Kourtis, P.; Magdău, I.-B.; Grey, C. P.; Csányi, G. Transferability of Datasets between Machine-Learning Interaction Potentials. *arXiv* **2024**.

https://doi.org/10.1021/acs.jctc.6c00403
J. Chem. Theory Comput. 2026, 22, 5174−5184

(50) Röcken, S.; Zavadlav, J. Enhancing Machine Learning Potentials through Transfer Learning across Chemical Elements. *J. Chem. Inf. Model* **2025**, *65* (14), 7406−7414.
(51) Smith, J. S.; Nebgen, B. T.; Zubatyuk, R.; Lubbers, N.; Devereux, C.; Barros, K.; Tretiak, S.; Isayev, O.; Roitberg, A. E. Approaching Coupled Cluster Accuracy with a General-Purpose Neural Network Potential through Transfer Learning. *Nat. Commun.* **2019**, *10* (1), 2903.
(52) Käser, S.; Boittier, E. D.; Upadhyay, M.; Meuwly, M. Transfer Learning to CCSD(T): Accurate Anharmonic Frequencies from Machine Learning Models. *J. Chem. Theory Comput.* **2021**, *17* (6), 3687−3699.
(53) Chen, M. S.; Lee, J.; Ye, H.-Z.; Berkelbach, T. C.; Reichman, D. R.; Markland, T. E. Data-Efficient Machine Learning Potentials from Transfer Learning of Periodic Correlated Electronic Structure Methods: Liquid Water at AFQMC, CCSD, and CCSD(T) Accuracy. *J. Chem. Theory Comput.* **2023**, *19* (14), 4510−4519.
(54) Zhang, L.; Han, J.; Wang, H.; Car, R.; E, W. Deep Potential Molecular Dynamics: A Scalable Model with the Accuracy of Quantum Mechanics. *Phys. Rev. Lett.* **2018**, *120* (14), 143001.
(55) Zhang, L.; Han, J.; Wang, H.; Saidi, W.; Car, R.; E, W. End-to-End Symmetry Preserving Inter-Atomic Potential Energy Model for Finite and Extended Systems. In *Advances in Neural Information Processing Systems 31*; Curran Associates, Inc., 2018.
(56) Zhang, Y.; Wang, H.; Chen, W.; Zeng, J.; Zhang, L.; Wang, H.; E, W. DP-GEN: A Concurrent Learning Platform for the Generation of Reliable Deep Learning Based Potential Energy Models. *Comput. Phys. Commun.* **2020**, *253*, 107206.
(57) Ceriotti, M.; Tribello, G. A.; Parrinello, M. Demonstrating the Transferability and the Descriptive Power of Sketch-Map. *J. Chem. Theory Comput.* **2013**, *9* (3), 1521−1532.
(58) Daru, J.; Forbert, H.; Behler, J.; Marx, D. Coupled Cluster Molecular Dynamics of Condensed Phase Systems Enabled by Machine Learning Potentials: Liquid Water Benchmark. *Phys. Rev. Lett.* **2022**, *129* (22), 226001.
(59) Ruth, M.; Gerbig, D.; Schreiner, P. R. Machine Learning of Coupled Cluster (T)-Energy Corrections via Delta (Δ)-Learning. *J. Chem. Theory Comput.* **2022**, *18* (8), 4846−4855.
(60) Qu, C.; Yu, Q.; Conte, R. L.; Houston, P.; Nandi, A. M.; Bomwan, J. A Δ-Machine Learning Approach for Force Fields, Illustrated by a CCSD(T) 4-Body Correction to the MB-Pol Water Potential. *Digit. Discovery* **2022**, *1* (5), 658−664.
(61) Mészáros, B. B.; Szabó, A.; Daru, J. Short-Range Δ-Machine Learning: A Cost-Efficient Strategy to Transfer Chemical Accuracy to Condensed Phase Systems. *J. Chem. Theory Comput.* **2025**, *21* (11), 5372−5381.
(62) O'Neill, N.; Shi, B. X.; Baldwin, W. J.; Witt, W. C.; Csányi, G.; Gale, J. D.; Michaelides, A.; Schran, C. Towards Routine Condensed Phase Simulations with Delta-Learned Coupled Cluster Accuracy: Application to Liquid Water. *J. Chem. Theory Comput.* **2025**, *21* (22), 11710−11720.
(63) Boittier, E. D.; Käser, S.; Meuwly, M. Roadmap to CCSD(T)-Quality Machine-Learned Potentials for Condensed Phase Simulations. *J. Chem. Theory Comput.* **2025**, *21* (18), 8683−8698.
(64) Zaverkin, V.; Holzmüller, D.; Schuldt, R.; Kästner, J. Predicting Properties of Periodic Systems from Cluster Data: A Case Study of Liquid Water. *J. Chem. Phys.* **2022**, *156* (11), 114103.
(65) Gawkowski, M. J.; Li, M.; Shi, B. X.; Kapil, V. The Good, the Bad, and the Ugly of Atomistic Learning for "Clusters-to-Bulk" Generalization. *Mach. Learn.: Sci. Technol.* **2026**, *7*, 025004.
(66) Zeng, J.; Giese, T. J.; Ekesan, ̧.; York, D. M. Development of Range-Corrected Deep Learning Potentials for Fast, Accurate Quantum Mechanical/Molecular Mechanical Simulations of Chemical Reactions in Solution. *J. Chem. Theory Comput.* **2021**, *17* (11), 6993−7009.
(67) Giese, T. J.; Zeng, J.; York, D. M. Transferability of MACE Graph Neural Network for Range Corrected Δ-Machine Learning Potential QM/MM Applications. *J. Phys. Chem. B* **2025**, *129* (22), 5477−5490.
(68) Morse, J. W.; Arvidson, R. S. The Dissolution Kinetics of Major Sedimentary Carbonate Minerals. *Earth-Sci. Rev.* **2002**, *58* (1), 51−84.
(69) Kellermeier, M.; Raiteri, P.; Berg, J. K.; Kempter, A.; Gale, J. D.; Gebauer, D. Entropy Drives Calcium Carbonate Ion Association. *ChemPhyschem* **2016**, *17* (21), 3535−3541.
(70) Chang, R.; Kim, S.; Lee, S.; Choi, S.; Kim, M.; Park, Y. Calcium Carbonate Precipitation for CO2 Storage and Utilization: A Review of the Carbonate Crystallization and Polymorphism. *Front. Energy Res.* **2017**, *5*, 5.
(71) Gebauer, D.; Völkel, A.; Cölfen, H. Stable Prenucleation Calcium Carbonate Clusters. *Science* **2008**, *322* (5909), 1819−1822.
(72) Raiteri, P.; Gale, J. D. Water Is the Key to Nonclassical Nucleation of Amorphous Calcium Carbonate. *J. Am. Chem. Soc.* **2010**, *132* (49), 17623−17634.
(73) Henzler, K.; Fetisov, E. O.; Galib, M.; Baer, M. D.; Legg, B. A.; Borca, C.; Xto, J. M.; Pin, S.; Fulton, J. L.; Schenter, G. K.; et al. Supersaturated Calcium Carbonate Solutions Are Classical. *Sci. Adv.* **2018**, *4* (1), No. eaao6283.
(74) Raiteri, P.; Demichelis, R.; Gale, J. D. Thermodynamically Consistent Force Field for Molecular Dynamics Simulations of Alkaline-Earth Carbonates and Their Aqueous Speciation. *J. Phys. Chem. C* **2015**, *119* (43), 24447−24458.
(75) Raiteri, P.; Schuitemaker, A.; Gale, J. D. Ion Pairing and Multiple Ion Binding in Calcium Carbonate Solutions Based on a Polarizable AMOEBA Force Field and Ab Initio Molecular Dynamics. *J. Phys. Chem. B* **2020**, *124* (17), 3568−3582.
(76) Piaggi, P. M.; Gale, J. D.; Raiteri, P. Ab Initio Machine-Learning Simulation of Calcium Carbonate from Aqueous Solutions to the Solid State. *Proc. Natl. Acad. Sci. U. S. A.* **2025**, *122* (41), No. e2415663122.
(77) Perdew, J. P.; Burke, K.; Ernzerhof, M. Generalized Gradient Approximation Made Simple. *Phys. Rev. Lett.* **1996**, *77* (18), 3865−3868.
(78) Zhang, Y.; Yang, W. Comment on ̀Generalized Gradient Approximation Made Simple". *Phys. Rev. Lett.* **1998**, *80* (4), 890−890.
(79) Becke, A. D.; Johnson, E. R. A Density-Functional Model of the Dispersion Interaction. *J. Chem. Phys.* **2005**, *123* (15), 154101.
(80) Grimme, S.; Antony, J.; Ehrlich, S.; Krieg, H. A Consistent and Accurate Ab Initio Parametrization of Density Functional Dispersion Correction (DFT-D) for the 94 Elements H-Pu. *J. Chem. Phys.* **2010**, *132* (15), 154104.
(81) Grimme, S.; Ehrlich, S.; Goerigk, L. Effect of the Damping Function in Dispersion Corrected Density Functional Theory. *J. Comput. Chem.* **2011**, *32* (7), 1456−1465.
(82) Sun, J.; Ruzsinszky, A.; Perdew, J. P. Strongly Constrained and Appropriately Normed Semilocal Density Functional. *Phys. Rev. Lett.* **2015**, *115* (3), 036402.
(83) Invernizzi, M.; Parrinello, M. Exploration vs Convergence Speed in Adaptive-Bias Enhanced Sampling. *J. Chem. Theory Comput.* **2022**, *18* (6), 3988−3996.
(84) Montero de Hijes, P.; Dellago, C.; Jinnouchi, R.; Kresse, G. Density Isobar of Water and Melting Temperature of Ice: Assessing Common Density Functionals. *J. Chem. Phys.* **2024**, *161* (13), 131102.
(85) Li, Y.; Yang, B.; Zhang, C.; Gomez, A.; Xie, P.; Chen, Y.; Piaggi, P. M.; Car, R. Assessment of First-Principles Methods in Modeling the Melting Properties of Water. *arXiv* **2025**.
(86) Ye, H.-Z.; Berkelbach, T. C. Periodic Local Coupled-Cluster Theory for Insulators and Metals. *J. Chem. Theory Comput.* **2024**, *20* (20), 8948−8959.
(87) Plummer, L. N.; Busenberg, E. The Solubilities of Calcite, Aragonite and Vaterite in CO2-H2O Solutions between 0 and 90°C, and an Evaluation of the Aqueous Model for the System CaCO3-CO2-H2O. *Geochim. Cosmochim. Acta* **1982**, *46* (6), 1011−1040.
(88) Aufort, J.; Raiteri, P.; Gale, J. D. Computational Insights into Mg2+ Dehydration in the Presence of Carbonate. *ACS Earth Space Chem.* **2022**, *6* (3), 733−745.
(89) Wen, X.; Boyn, J.-N.; Martirez, J. M. P.; Zhao, Q.; Carter, E. A. Strategies to Obtain Reliable Energy Landscapes from Embedded Multireference Correlated Wavefunction Methods for Surface Reactions. *J. Chem. Theory Comput.* **2024**, *20* (14), 6037−6048.

https://doi.org/10.1021/acs.jctc.6c00403
J. Chem. Theory Comput. 2026, 22, 5174−5184

(90) Kresse, G.; Joubert, D. From Ultrasoft Pseudopotentials to the Projector Augmented-Wave Method. *Phys. Rev. B* **1999**, *59* (3), 1758−1775.
(91) Kresse, G.; Hafner, J. Ab Initio Molecular Dynamics for Liquid Metals. *Phys. Rev. B* **1993**, *47* (1), 558−561.
(92) Kuang, Y.; Carter, E. A. *VASPEmbedding*. https://github.com/EACcodes/VASPEmbedding.
(93) Wu, Q.; Yang, W. A Direct Optimization Method for Calculating Density Functionals and Exchange−Correlation Potentials from Electron Densities. *J. Chem. Phys.* **2003**, *118* (6), 2498−2509.
(94) Yu, K.; Libisch, F.; Carter, E. A. Implementation of Density Functional Embedding Theory within the Projector-Augmented-Wave Method and Applications to Semiconductor Defect States. *J. Chem. Phys.* **2015**, *143* (10), 102806.
(95) Dunning, T. H. Gaussian Basis Sets for Use in Correlated Molecular Calculations. I. The Atoms Boron through Neon and Hydrogen. *J. Chem. Phys.* **1989**, *90* (2), 1007−1023.
(96) Krauter, C. M.; Carter, E. A. *EmbeddingIntegralGenerator*. https://github.com/EACcodes/EmbeddingIntegralGenerator.
(97) Sun, Q.; Zhang, X.; Banerjee, S.; Bao, P.; Barbry, M.; Blunt, N. S.; Bogdanov, N. A.; Booth, G. H.; Chen, J.; Cui, Z.-H.; Eriksen, J. J.; Gao, Y.; Guo, S.; Hermann, J.; Hermes, M. R.; Koh, K.; Koval, P.; Lehtola, S.; Li, Z.; Liu, J.; Mardirossian, N.; McClain, J. D.; Motta, M.; Mussard, B.; Pham, H. Q.; Pulkin, A.; Purwanto, W.; Robinson, P. J.; Ronca, E.; Sayfutyarova, E. R.; Scheurer, M.; Schurkus, H. F.; Smith, J. E. T.; Sun, C.; Sun, S.-N.; Upadhyay, S.; Wagner, L. K.; Wang, X.; White, A.; Whitfield, J. D.; Williamson, M. J.; Wouters, S.; Yang, J.; Yu, J. M.; Zhu, T.; Berkelbach, T. C.; Sharma, S.; Sokolov, A. Y.; Chan, G. K.-L. Recent Developments in the PySCF Program Package. *J. Chem. Phys.* **2020**, *153* (2), 024109.
(98) PySCF *pyscf-forge is a staging ground for code that may be suitable for pyscf-core*. https://github.com/pyscf/pyscf-forge.
(99) Zeng, J.; Zhang, D.; Peng, A.; Zhang, X.; He, S.; Wang, Y.; Liu, X.; Bi, H.; Li, Y.; Cai, C.; Zhang, C.; Du, Y.; Zhu, J.-X.; Mo, P.; Huang, Z.; Zeng, Q.; Shi, S.; Qin, X.; Yu, Z.; Luo, C.; Ding, Y.; Liu, Y.-P.; Shi, R.; Wang, Z.; Bore, S. L.; Chang, J.; Deng, Z.; Ding, Z.; Han, S.; Jiang, W.; Ke, G.; Liu, Z.; Lu, D.; Muraoka, K.; Oliaei, H.; Singh, A. K.; Que, H.; Xu, W.; Xu, Z.; Zhuang, Y.-B.; Dai, J.; Giese, T. J.; Jia, W.; Xu, B.; York, D. M.; Zhang, L.; Wang, H. DeePMD-Kit v3: A Multiple-Backend Framework for Machine Learning Potentials. *J. Chem. Theory Comput.* **2025**, *21* (9), 4375−4385.
(100) Thompson, A. P.; Aktulga, H. M.; Berger, R.; Bolintineanu, D. S.; Brown, W. M.; Crozier, P. S.; in't Veld, P. J.; Kohlmeyer, A.; Moore, S. G.; Nguyen, T. D.; Shan, R.; Stevens, M. J.; Tranchida, J.; Trott, C.; Plimpton, S. J. LAMMPS - a Flexible Simulation Tool for Particle-Based Materials Modeling at the Atomic, Meso, and Continuum Scales. *Comput. Phys. Commun.* **2022**, *271*, 108171.
(101) Tribello, G. A.; Bonomi, M.; Branduardi, D.; Camilloni, C.; Bussi, G. PLUMED 2: New Feathers for an Old Bird. *Comput. Phys. Commun.* **2014**, *185* (2), 604−613.
(102) Carter, E. A.; Ciccotti, G.; Hynes, J. T.; Kapral, R. Constrained Reaction Coordinate Dynamics for the Simulation of Rare Events. *Chem. Phys. Lett.* **1989**, *156* (5), 472−477.
(103) Den Otter, W. K.; Briels, W. J. Free Energy from Molecular Dynamics with Multiple Constraints. *Mol. Phys.* **2000**, *98* (12), 773−781.

https://doi.org/10.1021/acs.jctc.6c00403
J. Chem. Theory Comput. 2026, 22, 5174−5184

Supporting Information: Transfer Learning Meets Embedded Correlated Wavefunction Theory for Chemically Accurate Molecular Simulations: Application to Calcium Carbonate Ion-Pairing

Xuezhi Bian[1] and Emily A. Carter[2,3]

[1]Department of Chemistry, Princeton University, Princeton, New Jersey 08544, United States

[2]Department of Mechanical and Aerospace Engineering, Princeton University, Princeton, New Jersey 08544, United States

[3]Andlinger Center for Energy and the Environment and Program in Applied and Computational Mathematics, Princeton University, Princeton, New Jersey 08544, United States

1. Details and Validation of Machine-Learned Interatomic Potentials

The baseline DFT-revPBE-D3(BJ)-MLIP models were trained using a "training-exploration-labeling" active-learning workflow. The initial training dataset for the baseline model was selected from 24 5-ps constrained AIMD trajectories sampled at fixed Ca-C distances ranging from 2.6 Å to 5.4 Å (2.6, 2.8, 2.85, 2.9, 3.0, 3.05, 3.1, 3.2, 3.3, 3.4, 3.45, 3.5, 3.6, 3.7, 3.75, 3.8, 4.0, 4.2, 4.4, 4.6, 4.8, 5.0, 5.2, and 5.5 Å). 100 structures were sampled evenly along each trajectory, yielding a total of 2400 configurations. At each active-learning iteration, four MLIPs were trained independently with different random initial weights to form a committee. For the DP models, we employed the standard short-range, smooth two-body descriptor with a cutoff radius of $r_c = 6$ Å. The embedding network consisted of three layers with 25, 50, and 100 neurons, and 12 axis neurons, while the fitting network comprised three layers of 240 neurons each. Each model was trained for 400,000 steps using an exponentially decaying learning rate, which decreased from 10^{-3} to 10^{-8}. During training, we scheduled the energy prefactor in the loss function to increase from 0.02 to 1, while the force prefactor was set to decrease from 1000 to 1. These hyperparameters follow standard settings used for DP models trained for aqueous systems.

For the exploration stage, enhanced-sampling MD simulations based on the Ca-C distance were performed. Configurations exhibiting force deviations between 0.05 and 0.15 eV/Å among the 4 models were identified as uncertain and added to the training set. At each iteration, up to 500 configurations were selected and single-point DFT reference calculations were performed to obtain reference energies and forces, which were then added to the training dataset.

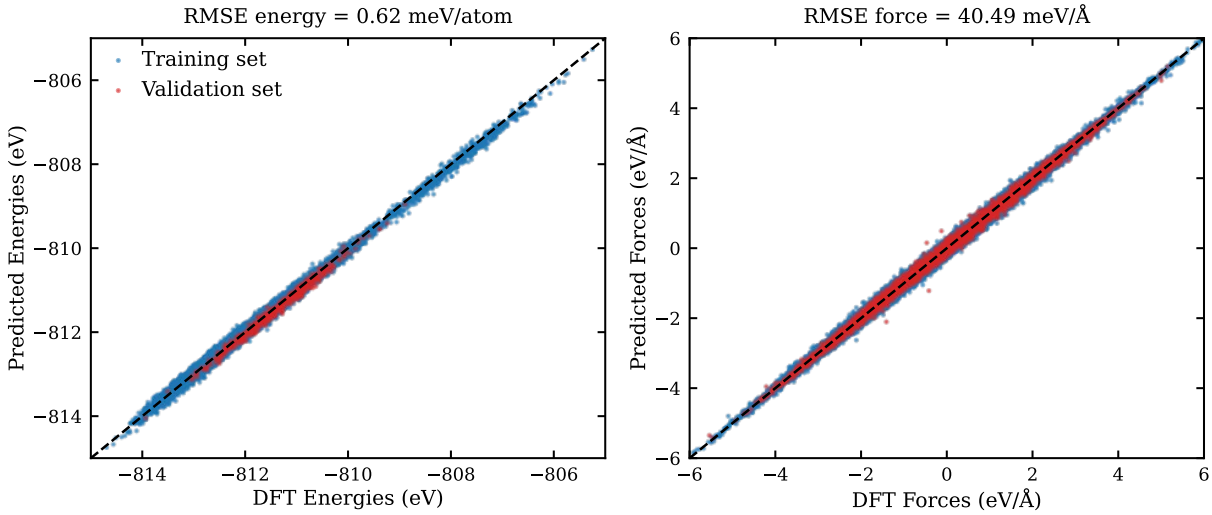

Figure S1 Comparison between DFT energies and forces and the baseline DFT-revPBE-D3(BJ) MLIP predicted energies and forces for both training and validation datasets. The model performs well on both datasets.

Active learning was considered converged after 12 iterations, because the difference between free-energy surfaces (FESs) computed in the last two active learning iterations was smaller than 0.2

kcal/mol across the entire sampled collective variable (CV) range, with a total of 6973 configurations accumulated. A final production model then was trained on this dataset for 1,000,000 ML steps to obtain the baseline DFT-revPBE-D3(BJ) model used in this work. The resulting model has a root-mean-square error (RMSE) of 0.62 meV/atom for energies and 40.49 meV/Å for forces on the training dataset. To validate the baseline model further, we performed 24 independent constrained MD simulations at the same fixed Ca-C distances as above for the initial training dataset, each 100 ps in length. 20 configurations were extracted from each trajectory at uniform time intervals, resulting in a validation set of 480 configurations. As shown in Fig. S1, the model exhibits errors in both energies and forces that are comparable to those observed in the training set.

Similarly, for the DFT-SCAN-MLIP model, the initial dataset of 500 configurations was randomly selected from the DFT-revPBE-D3(BJ) training set, and the same active-learning procedure was applied until convergence, resulting in a total of 7581 configurations. The final DFT-SCAN-MLIP model achieves an RMSE of 0.46 meV/atom for energies and 42.25 meV/Å for forces on the training dataset.

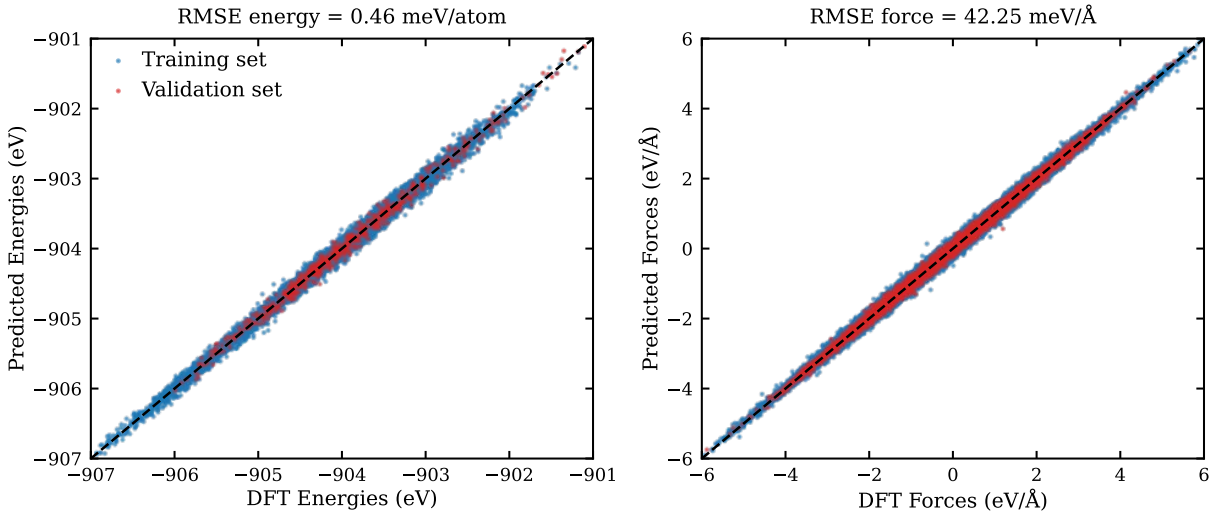

Figure S2 Same as Fig. S1, but for the DFT-SCAN-MLIP model. The model performs well on both training and validation datasets.

During transfer learning, the model was initialized from the baseline revPBE-D3(BJ) model. The embedding neural network was frozen, and we chose to apply a reduced learning rate starting from 10^{-4} decreasing to 10^{-8} over 400,000 steps. Because high-level ECW data contain only energies, we fixed the energy prefactor in the loss function to 1 and the force prefactor to 0. A larger learning rate or updating all parameters leads to catastrophic forgetting of the pretrained baseline model and results in unstable MD dynamics. Conversely, freezing too many parameters prevents the model from learning meaningful high-level corrections, causing it to behave similarly to the

baseline DFT model. The chosen empirical settings therefore represent a balance between retaining the baseline representation and incorporating the ECW-level information effectively.

2. Comparison of Enhanced Sampling Methods

For all FESs reported in the main text, we employed the on-the-fly probability enhanced sampling (OPES) method using a metadynamics-like target distribution,[1] in the LAMMPS[2] package with the PLUMED[3] plugin. During sampling, the bias potential was updated every 500 steps, with a maximum bias barrier of 50 kJ/mol. To prevent the Ca-C distance from sampling unphysically large values, we applied an upper wall at 6 Å with a harmonic force constant of 1000 kJ/mol/nm^2 which corresponds to approximately half the length of the simulation cell. All simulations were performed in the NVT ensemble using a canonical sampling with velocity-rescaling (CSVR) thermostat,[4] with a relaxation time of 100 ps. We used a 0.5 fs timestep, and we assigned a mass of 2 amu to hydrogen atoms for stable integration. This modification does not affect the resulting FES, which is an equilibrium observable independent of the particle masses.

For each FES, four independent trajectories of 2 ns were generated to ensure statistical reliability. The final free energy at a given $\boldsymbol{R}_{\mathrm{Ca-C}} = \boldsymbol{s}$ was calculated using standard reweighting of biased trajectories:

$$F(\boldsymbol{s}) = -\frac{1}{\beta}\ln\left(\frac{\left\langle \delta(\boldsymbol{R}_{\mathrm{Ca-C}} - \boldsymbol{s}) e^{\beta V(\boldsymbol{R})} \right\rangle}{\left\langle e^{\beta V(\boldsymbol{R})} \right\rangle}\right) \tag{S1}$$

where $\beta = 1/k_B T$, $V(\boldsymbol{R})$ is the bias potential at configuration $\boldsymbol{R}$, and $\langle\cdot\rangle$ represents the statistical average over the biased simulation.

Previous studies employing different enhanced-sampling techniques have reported noticeably different FES profiles even when using comparable electronic-structure methods. To assess the influence of the sampling method, we also computed the FES using the blue-moon ensemble (BME)[5,6] with our DFT-revPBE-D3(BJ) baseline MLIP model. 29 constrained trajectories of 400 ps each were propagated with the CP2K package,[7] with constraint values evenly spaced between $R_{\mathrm{Ca-C}} = 2.6$ to 5.4 Å. All BME simulations used the same CSVR thermostat parameters as the OPES simulations, with a 0.25 fs timestep and a hydrogen mass of 1 amu (because the mass cannot be set to 2 amu in CP2K to run these simulations, using a shorter timestep compensates for having to use the smaller mass). The free energy was then obtained from integrating the average constraint force according to

$$F(s) = \int_{s_0}^{s} ds\, \langle \lambda(s) \rangle - \frac{2}{\beta}\ln(s) \tag{S2}$$

where $\langle \lambda(s) \rangle$ is the statistical average of the Lagrange multiplier in the SHAKE algorithm[8] and the second term in Eq. (S2) is the entropy contribution from the Jacobi factor.

In Fig. S2, we compare the FES obtained from both the OPES and BME approaches. The two methods agree well, indicating that the ion-pairing FES is insensitive to the choice of enhanced sampling techniques. Nevertheless, both OPES and BME require relatively long sampling times to achieve convergence, which may help explain the discrepancies observed in some earlier AIMD-based studies.

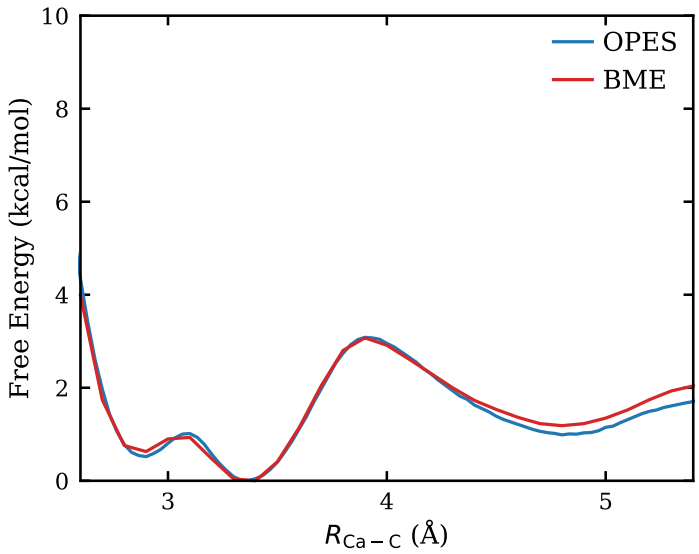

Figure S3 Free-energy surfaces computed using the BME and OPES enhanced-sampling methods. The two methods show excellent agreement.

3. Temperature Effects

Here we report the FES computed using the baseline DFT-revPBE-D3(BJ) MLIP model at different temperatures. As shown in Fig. S4, the temperature dependence in the bidentate and monodentate CIP regions is small, reflecting that the strong cation-ligand binding dominates the energetics in these configurations. In contrast, at the SSIP region and beyond, temperature effects become larger due to the increasing importance of entropy of the water configurations near and shared between the ion pair. Overall, the temperature dependence of the FES remains relatively small in the 300-330 K range. Looking forward, it will be interesting to explore the temperature dependence of the FES at higher temperatures using chemically accurate ECW-TL MLIP models to fully assess the role of entropic contributions.

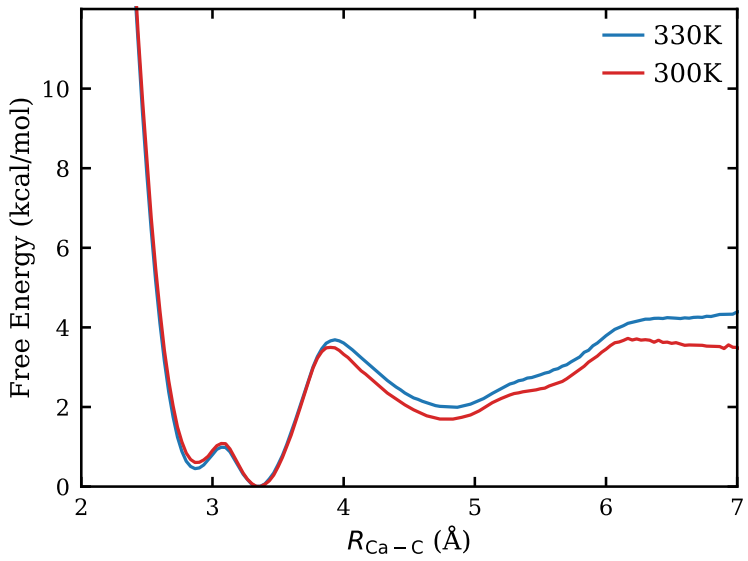

Figure S4 Free-energy surfaces computed at two temperatures with the DFT-revPBE-D3(BJ) MLIP model. The profiles show a relatively small temperature dependence at or near room-temperature.

4. Details and Convergence Tests for Periodic ECW Calculations

For the embedding potential generation, a 216 × 216 × 216 real-space grid is used for the fast Fourier transform (FFT) in the plane-wave DFT calculation, and the parameter F_{Corr} that controls the region of derivative corrections is set to 0.70. Within the projector augmented-wave (PAW) density functional embedding theory (DFET) method, the derivative correction is only evaluated for points within $F_{\mathrm{Corr}}R_{\mathrm{aug}}$, where R_{aug} is the core radius.[9] The embedding potential V_{emb} is optimized by maximizing the extended Wu-Yang functional to a gradient threshold of 10^{-5}. Once the embedding potential is optimized, we project it onto a Gaussian-type orbital (GTO) basis using the EmbeddingIntegralGenerator code[10] to perform ECW calculation:

$$V_{\mu\nu}^{\mathrm{emb}} = \langle \mu | \hat{V}_{\mathrm{emb}} | \nu \rangle \tag{S3}$$

where $V_{\mu\nu}^{\mathrm{emb}}$ represents the one-electron embedding potential integral between atomic orbitals μ and ν. The ECW Hamiltonian can be expressed as

$$\hat{H}_{\mathrm{ECW}} = \hat{H}_{\mathrm{CW}} + \hat{V}_{\mathrm{emb}}. \tag{S4}$$

where $\hat{H}_{\mathrm{CW}}$ is the corresponding correlated wavefunction Hamiltonian of the cluster.

One issue with the current cell and cluster size is that the cluster sits too close to its periodic images. Although the embedding potential correctly accounts for interactions between the cluster and the environment - including all periodic replicas of the environment - it does not include the interactions between the cluster itself and its periodic images. To eliminate this artifact, we therefore used periodic GTO-based methods for the embedded DFT and ECW calculations with the ECW Hamiltonian defined in Eq. (S4), ensuring that the interactions between the cluster and both the periodic environment and cluster images are correctly included. We note this is the first time that the ECW framework has included these periodic images. Largely, the ECW method has been used to study metallic systems, which screen interactions rapidly, such that there was no need to include periodic images of the embedded clusters. But in lower dielectric constant condensed matter, it is fortunate that periodic CW methods and codes now can be utilized with ECW to properly account for all periodic interactions.

In PySCF,[11] the cell precision parameter controls the accuracy of periodic GTO integrals by setting the FFT grid, kinetic-energy cutoff, and lattice-summation cutoff. Figure S5 shows the convergence of SCF energies of periodic GTO DFT calculations with respect to the precision parameter. A precision value of 10^{-10} was used in this work, which yields convergence to better than approximately 0.001 kcal/mol or 1.6×10^{-6} Hartree.

For all periodic GTO calculations in this work, we used a large cc-pVTZ[12] basis set and a def2-TZVPP auxiliary basis[13] for density fitting to accelerate computations. We used a Gaussian smearing of 0.1 eV to stabilize SCF convergence and the SCF energies were converged to a threshold to 10^{-8} Hartree.

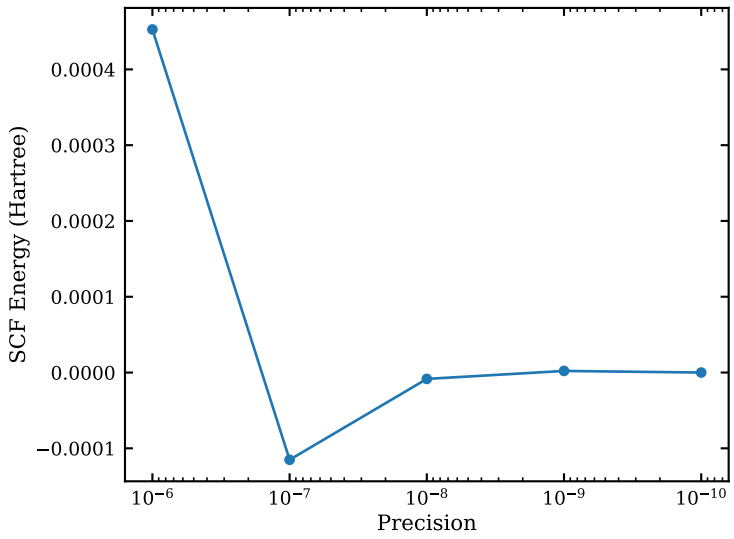

Figure S5 SCF energies as a function of the precision parameter in periodic GTO DFT calculations. A precision parameter of 10^{-10} provides good convergence. The energy zero is defined as the SCF energy calculated at 10^{-10}.

The embedded periodic GTO method was validated against the embedded periodic planewave (PW) method at the DFT-SCAN level (with periodic PW DFT-revPBE-D3(BJ) as the low-level theory for the total system). In Fig. S6, we present an energy parity plot comparing embedded periodic GTO DFT-SCAN and embedded periodic PW DFT-SCAN energies for the dataset used in the first fine-tuning iteration described in the main text (~700 configurations). The two methods agree quite well, considering these are total absolute energies (the error will be far less for actual energy observables, which are energy differences).

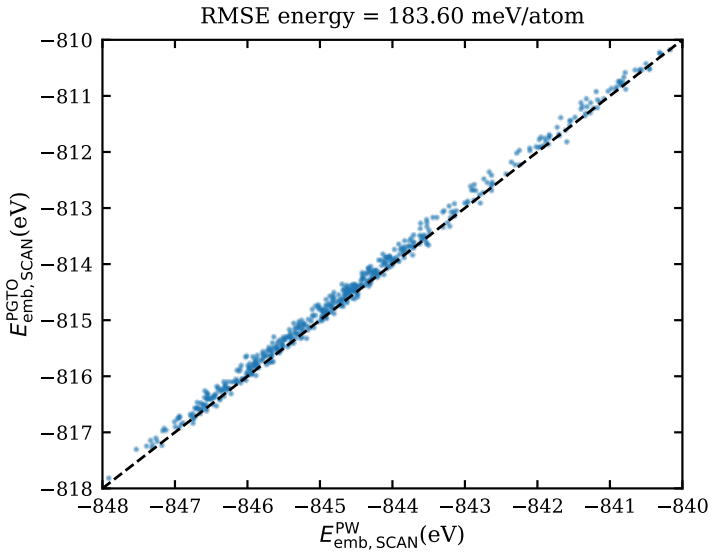

Figure S6 Comparison between embedded periodic GTO DFT-SCAN and embedded periodic PW DFT-SCAN energies, showing satisfactory agreement in total energies.

For the embedded periodic GTO MP2 and LNO-CCSD(T) calculations, after achieving convergence at the periodic Hartree-Fock level, we froze the inner-core 1s orbitals of C and O, and the 1s, 2s, and 2p orbitals of Ca for the later correlated calculations. For the embedded periodic LNO-CCSD(T) calculations,[14] first the canonical HF orbitals were localized using the Pipek-Mezey localization[15] to generate local orbitals and define fragments. The local subspace was defined by freezing occupied and virtual natural orbitals with eigenvalues below user-defined thresholds η_{occ} (η_{vir}) for each local fragments. The periodic LNO-CCSD(T) calculation then was carried out in the resulting truncated orbital space.[14] Note that at the $\eta_{\mathrm{occ}} = \eta_{\mathrm{vir}} = 0$ limit, LNO-CCSD(T) reduces to canonical CCSD(T). Here we fix the ratio $\eta_{\mathrm{occ}}/\eta_{\mathrm{vir}} = 10$ as recommended for molecular LNO-CC[16] and scan η_{vir} to analyze the convergence behavior.

The final embedded periodic LNO-CCSD(T) energies as a function of η_{vir} are plotted in Fig. S6.

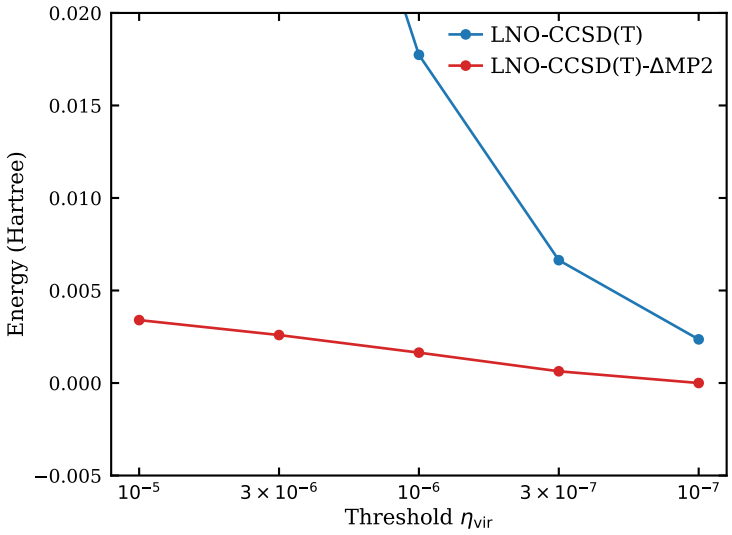

Figure S7 Embedded periodic LNO-CCSD(T) and periodic LNO-CCSD(T)-ΔMP2 energies as function of active space threshold η_{vir}. The energy zero is defined as the LNO-CCSD(T)- ΔMP2 energy calculated at $\eta_{\mathrm{vir}} = 10^{-7}$.

Although the direct LNO-CCSD(T) converges slowly with respect to the virtual space threshold, the MP2-corrected LNO-CCSD(T)-ΔMP2 defined as:

$$E_{\mathrm{LNO-CCSD(T)-\Delta MP2}} = E_{\mathrm{LNO-CCSD(T)}} + (E_{\mathrm{MP2}} - E_{\mathrm{LNO-MP2}}) \tag{S5}$$

converges to within 1 kcal/mol (or 1.6×10^{-3} Hartree) at $\eta_{\mathrm{vir}} = 10^{-6}$. Here, the MP2 correction term in parentheses in Eq. S5 represents the energy difference between periodic MP2 and periodic LNO-MP2. We therefore set $\eta_{\mathrm{vir}} = 10^{-6}$ as a compromise between computational cost and accuracy and use $E_{\mathrm{LNO-CCSD(T)-\Delta MP2}}$ as our reference energy in ECW-TL training.

5. Comparison Between ECW-TL and Direct Cluster Δ-Learning

Finally, we demonstrate the power of our ECW-TL framework by comparing it to the traditional Δ-learning approach. For the direct cluster Δ-learning approach, the high-level reference energy used to finetune baseline MLIP is defined as

$$E_{\Delta-\text{learning}} = E_{\text{baseline}} + \left(E^{\text{cluster}}_{\text{high-level}} - E^{\text{cluster}}_{\text{baseline}}\right) \quad \text{(S6)}$$

where the correction is constructed from an isolated cluster. The key difference between this Δ-learning approach and our ECW-TL framework is that it neglects all interactions between the selected cluster and the surrounding environment. We used the same configurations as in the transfer learning of our embedded-DFT-SCAN model in the main text, but with reference energies redefined according to Eq. (S6) to finetune the baseline DFT-revPBE-D3(BJ) model.

In Fig. S7, we plot the FES computed from both the embedded DFT-SCAN model and the direct cluster Δ-learning approach. Our embedded model clearly is more accurate than the isolated cluster model under the same transfer-learning setup. This result highlights the importance of properly accounting for system-environment interactions when fine-tuning MLIP models.

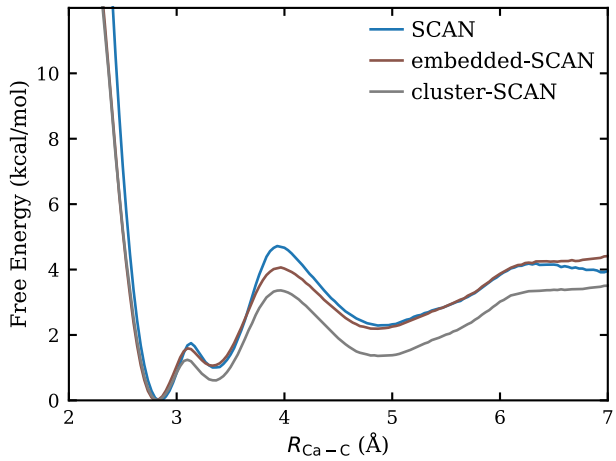

Figure S8 Free-energy surfaces computed from the two transfer-learning DFT-SCAN models compared with the DFT-SCAN reference model.

6. Comparison of DFT-based FESs with previous related studies

The FESs computed from our DFT-revPBE-D3(BJ) and DFT-SCAN models are compared in Fig. S9 with previous studies by Boyn et al.[17] and Piaggi et al. [18] . We find that the DFT-revPBE-D3(BJ)-MLIP-MD results in this work are in *qualitative* agreement with the DFT-revPBE-D3(BJ)-MD results of Boyn et al. in the bidentate and monodentate CIP regions. However, the DFT-MD results in Ref. 17 predict a significantly lower minimum in the SSHIP region, in disagreement with our results. These differences likely arise from limited sampling possible in the previous DFT-MD simulations, where each constrained MD trajectory was sampled for only 10 ps, which may not have been sufficient to achieve full convergence. This comparison highlights the advantage of MLIP-based simulations in obtaining well-converged FESs for ion-pairing systems.

For the MLIP-DFT-SCAN-based results, the model in this work and that of Ref. 18 again agree qualitatively. The remaining quantitative differences may arise from several factors. First, Piaggi et al. employed norm-conserving pseudopotentials, whereas we use all-electron, frozen-core PAW potentials. Second, their simulations were performed in the NPT ensemble, while ours are conducted in the NVT ensemble. Third, the model of Piaggi et al. was trained on a broader set of configurations spanning multiple processes, which may compromise accuracy for ion pairing compared to our model specifically trained for this system.

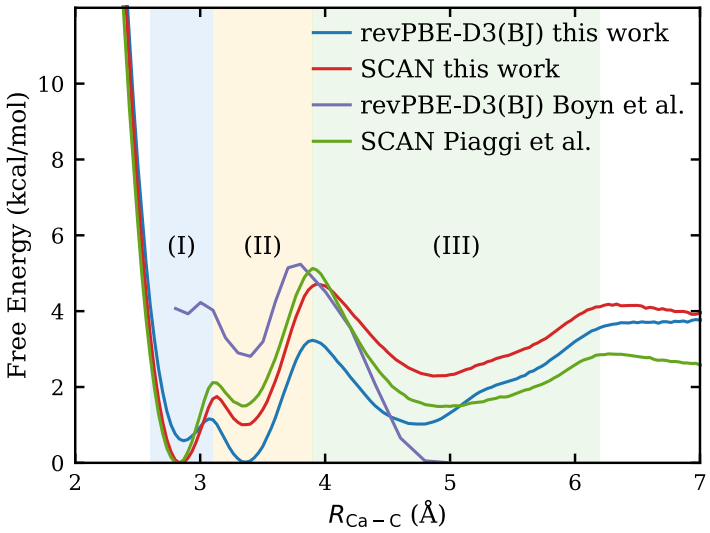

Figure S9 Free-energy surfaces computed from our two DFT-MLIP models compared with previous studies in Refs. 17 (revPBE-D3(BJ)-MD only) and 18 (SCAN-MLIP-MD only).

References

(1) Invernizzi, M.; Parrinello, M. Exploration vs Convergence Speed in Adaptive-Bias Enhanced Sampling. *J. Chem. Theory Comput.* **2022**, *18* (6), 3988–3996. https://doi.org/10.1021/acs.jctc.2c00152.

(2) Thompson, A. P.; Aktulga, H. M.; Berger, R.; Bolintineanu, D. S.; Brown, W. M.; Crozier, P. S.; in 't Veld, P. J.; Kohlmeyer, A.; Moore, S. G.; Nguyen, T. D.; Shan, R.; Stevens, M. J.; Tranchida, J.; Trott, C.; Plimpton, S. J. LAMMPS - a Flexible Simulation Tool for Particle-Based Materials Modeling at the Atomic, Meso, and Continuum Scales. *Comput. Phys. Commun.* **2022**, *271*, 108171. https://doi.org/10.1016/j.cpc.2021.108171.

(3) Tribello, G. A.; Bonomi, M.; Branduardi, D.; Camilloni, C.; Bussi, G. PLUMED 2: New Feathers for an Old Bird. *Comput. Phys. Commun.* **2014**, *185* (2), 604–613. https://doi.org/10.1016/j.cpc.2013.09.018.

(4) Bussi, G.; Donadio, D.; Parrinello, M. Canonical Sampling through Velocity Rescaling. *J. Chem. Phys.* **2007**, *126* (1), 014101. https://doi.org/10.1063/1.2408420.

(5) Carter, E. A.; Ciccotti, G.; Hynes, J. T.; Kapral, R. Constrained Reaction Coordinate Dynamics for the Simulation of Rare Events. *Chem. Phys. Lett.* **1989**, *156* (5), 472–477. https://doi.org/10.1016/S0009-2614(89)87314-2.

(6) DEN OTTER, W. K.; BRIELS, W. J. Free Energy from Molecular Dynamics with Multiple Constraints. *Mol. Phys.* **2000**, *98* (12), 773–781. https://doi.org/10.1080/00268970009483348.

(7) Kühne, T. D.; Iannuzzi, M.; Del Ben, M.; Rybkin, V. V.; Seewald, P.; Stein, F.; Laino, T.; Khaliullin, R. Z.; Schütt, O.; Schiffmann, F.; Golze, D.; Wilhelm, J.; Chulkov, S.; Bani-Hashemian, M. H.; Weber, V.; Borštnik, U.; Taillefumier, M.; Jakobovits, A. S.; Lazzaro, A.; Pabst, H.; Müller, T.; Schade, R.; Guidon, M.; Andermatt, S.; Holmberg, N.; Schenter, G. K.; Hehn, A.; Bussy, A.; Belleflamme, F.; Tabacchi, G.; Glöß, A.; Lass, M.; Bethune, I.; Mundy, C. J.; Plessl, C.; Watkins, M.; VandeVondele, J.; Krack, M.; Hutter, J. CP2K: An Electronic Structure and Molecular Dynamics Software Package - Quickstep: Efficient and Accurate Electronic Structure Calculations. *J. Chem. Phys.* **2020**, *152* (19), 194103. https://doi.org/10.1063/5.0007045.

(8) Ryckaert, J.-P.; Ciccotti, G.; Berendsen, H. J. C. Numerical Integration of the Cartesian Equations of Motion of a System with Constraints: Molecular Dynamics of *n*-Alkanes. *J. Comput. Phys.* **1977**, *23* (3), 327–341. https://doi.org/10.1016/0021-9991(77)90098-5.

(9) Yu, K.; Libisch, F.; Carter, E. A. Implementation of Density Functional Embedding Theory within the Projector-Augmented-Wave Method and Applications to Semiconductor Defect States. *J. Chem. Phys.* **2015**, *143* (10), 102806. https://doi.org/10.1063/1.4922260.

(10) Krauter, C. M.; Carter, E. A. EmbeddingIntegralGenerator. https://github.com/EACcodes/EmbeddingIntegralGenerator.

(11) Sun, Q.; Zhang, X.; Banerjee, S.; Bao, P.; Barbry, M.; Blunt, N. S.; Bogdanov, N. A.; Booth, G. H.; Chen, J.; Cui, Z.-H.; Eriksen, J. J.; Gao, Y.; Guo, S.; Hermann, J.; Hermes, M. R.; Koh, K.; Koval, P.; Lehtola, S.; Li, Z.; Liu, J.; Mardirossian, N.; McClain, J. D.; Motta, M.; Mussard, B.; Pham, H. Q.; Pulkin, A.; Purwanto, W.; Robinson, P. J.; Ronca, E.; Sayfutyarova, E. R.; Scheurer, M.; Schurkus, H. F.; Smith, J. E. T.; Sun, C.; Sun, S.-N.; Upadhyay, S.; Wagner, L. K.; Wang, X.; White, A.; Whitfield, J. D.; Williamson, M. J.; Wouters, S.; Yang, J.; Yu, J. M.; Zhu, T.; Berkelbach, T. C.; Sharma, S.; Sokolov, A. Yu.; Chan, G. K.-L. Recent Developments

in the PySCF Program Package. *J. Chem. Phys.* **2020**, *153* (2), 024109. https://doi.org/10.1063/5.0006074.
(12) Dunning, T. H. Gaussian Basis Sets for Use in Correlated Molecular Calculations. I. The Atoms Boron through Neon and Hydrogen. *J. Chem. Phys.* **1989**, *90* (2), 1007–1023. https://doi.org/10.1063/1.456153.
(13) Weigend, F.; Ahlrichs, R. Balanced Basis Sets of Split Valence, Triple Zeta Valence and Quadruple Zeta Valence Quality for H to Rn: Design and Assessment of Accuracy. *Phys. Chem. Chem. Phys.* **2005**, *7* (18), 3297–3305. https://doi.org/10.1039/B508541A.
(14) Ye, H.-Z.; Berkelbach, T. C. Periodic Local Coupled-Cluster Theory for Insulators and Metals. *J. Chem. Theory Comput.* **2024**, *20* (20), 8948–8959. https://doi.org/10.1021/acs.jctc.4c00936.
(15) Pipek, J.; Mezey, P. G. A Fast Intrinsic Localization Procedure Applicable for Ab Initio and Semiempirical Linear Combination of Atomic Orbital Wave Functions. *J. Chem. Phys.* **1989**, *90* (9), 4916–4926. https://doi.org/10.1063/1.456588.
(16) Rolik, Z.; Szegedy, L.; Ladjánszki, I.; Ladóczki, B.; Kállay, M. An Efficient Linear-Scaling CCSD(T) Method Based on Local Natural Orbitals. *J. Chem. Phys.* **2013**, *139* (9), 094105. https://doi.org/10.1063/1.4819401.
(17) Boyn, J.-N.; Carter, E. A. Characterizing the Mechanisms of Ca and Mg Carbonate Ion-Pair Formation with Multi-Level Molecular Dynamics/Quantum Mechanics Simulations. *J. Phys. Chem. B* **2023**, *127* (50), 10824–10832. https://doi.org/10.1021/acs.jpcb.3c05369.
(18) Piaggi, P. M.; Gale, J. D.; Raiteri, P. Ab Initio Machine-Learning Simulation of Calcium Carbonate from Aqueous Solutions to the Solid State. *Proc. Natl. Acad. Sci.* **2025**, *122* (41), e2415663122. https://doi.org/10.1073/pnas.2415663122.

Supporting Information: Transfer Learning Meets Embedded Correlated Wavefunction Theory for Chemically Accurate Molecular Simulations: Application to Calcium Carbonate Ion-Pairing

Xuezhi Bian[1] and Emily A. Carter[2,3]

[1]Department of Chemistry, Princeton University, Princeton, New Jersey 08544, United States

[2]Department of Mechanical and Aerospace Engineering, Princeton University, Princeton, New Jersey 08544, United States

[3]Andlinger Center for Energy and the Environment and Program in Applied and Computational Mathematics, Princeton University, Princeton, New Jersey 08544, United States

1. Details and Validation of Machine-Learned Interatomic Potentials

The baseline DFT-revPBE-D3(BJ)-MLIP models were trained using a "training-exploration-labeling" active-learning workflow. The initial training dataset for the baseline model was selected from 24 5-ps constrained AIMD trajectories sampled at fixed Ca-C distances ranging from 2.6 Å to 5.4 Å (2.6, 2.8, 2.85, 2.9, 3.0, 3.05, 3.1, 3.2, 3.3, 3.4, 3.45, 3.5, 3.6, 3.7, 3.75, 3.8, 4.0, 4.2, 4.4, 4.6, 4.8, 5.0, 5.2, and 5.5 Å). 100 structures were sampled evenly along each trajectory, yielding a total of 2400 configurations. At each active-learning iteration, four MLIPs were trained independently with different random initial weights to form a committee. For the DP models, we employed the standard short-range, smooth two-body descriptor with a cutoff radius of $r_c = 6$ Å. The embedding network consisted of three layers with 25, 50, and 100 neurons, and 12 axis neurons, while the fitting network comprised three layers of 240 neurons each. Each model was trained for 400,000 steps using an exponentially decaying learning rate, which decreased from 10^{-3} to 10^{-8}. During training, we scheduled the energy prefactor in the loss function to increase from 0.02 to 1, while the force prefactor was set to decrease from 1000 to 1. These hyperparameters follow standard settings used for DP models trained for aqueous systems.

For the exploration stage, enhanced-sampling MD simulations based on the Ca-C distance were performed. Configurations exhibiting force deviations between 0.05 and 0.15 eV/Å among the 4 models were identified as uncertain and added to the training set. At each iteration, up to 500 configurations were selected and single-point DFT reference calculations were performed to obtain reference energies and forces, which were then added to the training dataset.

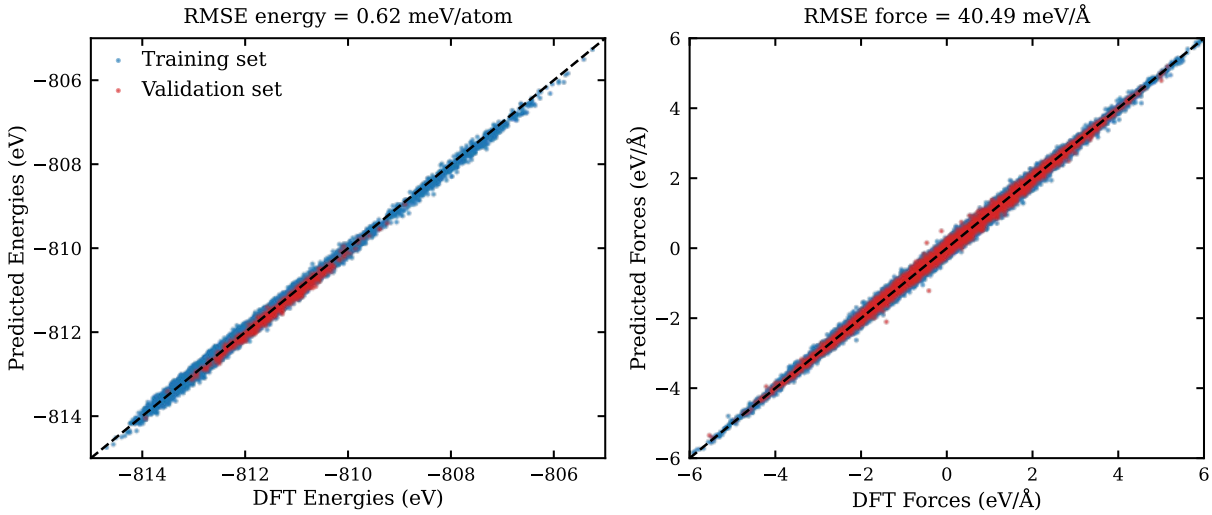

Figure S1 Comparison between DFT energies and forces and the baseline DFT-revPBE-D3(BJ) MLIP predicted energies and forces for both training and validation datasets. The model performs well on both datasets.

Active learning was considered converged after 12 iterations, because the difference between free-energy surfaces (FESs) computed in the last two active learning iterations was smaller than 0.2

kcal/mol across the entire sampled collective variable (CV) range, with a total of 6973 configurations accumulated. A final production model then was trained on this dataset for 1,000,000 ML steps to obtain the baseline DFT-revPBE-D3(BJ) model used in this work. The resulting model has a root-mean-square error (RMSE) of 0.62 meV/atom for energies and 40.49 meV/Å for forces on the training dataset. To validate the baseline model further, we performed 24 independent constrained MD simulations at the same fixed Ca-C distances as above for the initial training dataset, each 100 ps in length. 20 configurations were extracted from each trajectory at uniform time intervals, resulting in a validation set of 480 configurations. As shown in Fig. S1, the model exhibits errors in both energies and forces that are comparable to those observed in the training set.

Similarly, for the DFT-SCAN-MLIP model, the initial dataset of 500 configurations was randomly selected from the DFT-revPBE-D3(BJ) training set, and the same active-learning procedure was applied until convergence, resulting in a total of 7581 configurations. The final DFT-SCAN-MLIP model achieves an RMSE of 0.46 meV/atom for energies and 42.25 meV/Å for forces on the training dataset.

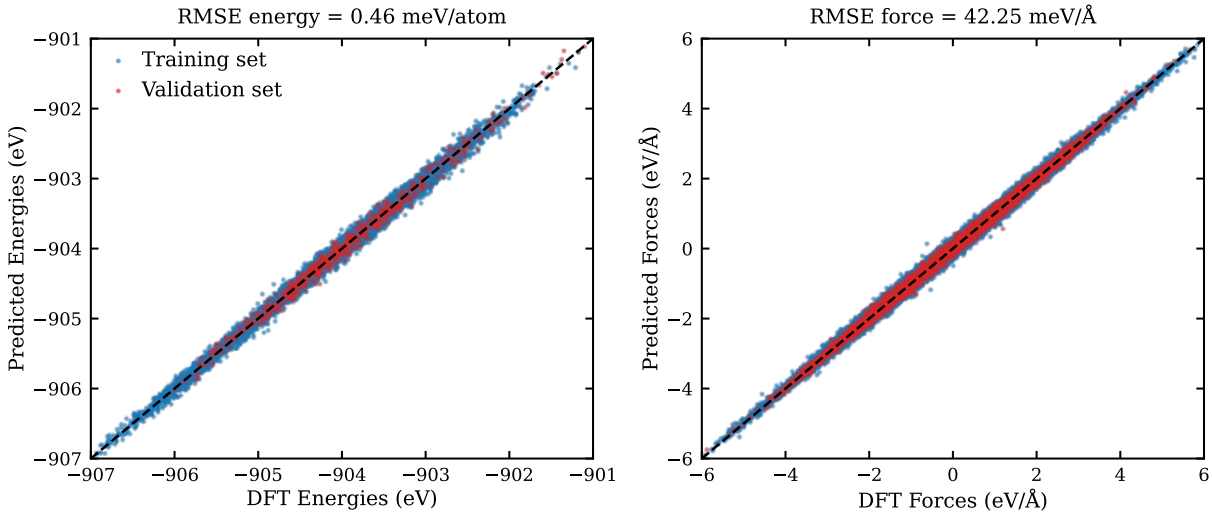

Figure S2 Same as Fig. S1, but for the DFT-SCAN-MLIP model. The model performs well on both training and validation datasets.

During transfer learning, the model was initialized from the baseline revPBE-D3(BJ) model. The embedding neural network was frozen, and we chose to apply a reduced learning rate starting from 10^{-4} decreasing to 10^{-8} over 400,000 steps. Because high-level ECW data contain only energies, we fixed the energy prefactor in the loss function to 1 and the force prefactor to 0. A larger learning rate or updating all parameters leads to catastrophic forgetting of the pretrained baseline model and results in unstable MD dynamics. Conversely, freezing too many parameters prevents the model from learning meaningful high-level corrections, causing it to behave similarly to the

baseline DFT model. The chosen empirical settings therefore represent a balance between retaining the baseline representation and incorporating the ECW-level information effectively.

2. Comparison of Enhanced Sampling Methods

For all FESs reported in the main text, we employed the on-the-fly probability enhanced sampling (OPES) method using a metadynamics-like target distribution,[1] in the LAMMPS[2] package with the PLUMED[3] plugin. During sampling, the bias potential was updated every 500 steps, with a maximum bias barrier of 50 kJ/mol. To prevent the Ca-C distance from sampling unphysically large values, we applied an upper wall at 6 Å with a harmonic force constant of 1000 kJ/mol/nm^2 which corresponds to approximately half the length of the simulation cell. All simulations were performed in the NVT ensemble using a canonical sampling with velocity-rescaling (CSVR) thermostat,[4] with a relaxation time of 100 ps. We used a 0.5 fs timestep, and we assigned a mass of 2 amu to hydrogen atoms for stable integration. This modification does not affect the resulting FES, which is an equilibrium observable independent of the particle masses.

For each FES, four independent trajectories of 2 ns were generated to ensure statistical reliability. The final free energy at a given $\boldsymbol{R}_{\mathrm{Ca-C}} = \boldsymbol{s}$ was calculated using standard reweighting of biased trajectories:

$$F(\boldsymbol{s}) = -\frac{1}{\beta}\ln\left(\frac{\left\langle \delta(\boldsymbol{R}_{\mathrm{Ca-C}} - \boldsymbol{s}) e^{\beta V(\boldsymbol{R})} \right\rangle}{\left\langle e^{\beta V(\boldsymbol{R})} \right\rangle}\right) \tag{S1}$$

where $\beta = 1/k_B T$, $V(\boldsymbol{R})$ is the bias potential at configuration $\boldsymbol{R}$, and $\langle\cdot\rangle$ represents the statistical average over the biased simulation.

Previous studies employing different enhanced-sampling techniques have reported noticeably different FES profiles even when using comparable electronic-structure methods. To assess the influence of the sampling method, we also computed the FES using the blue-moon ensemble (BME)[5,6] with our DFT-revPBE-D3(BJ) baseline MLIP model. 29 constrained trajectories of 400 ps each were propagated with the CP2K package,[7] with constraint values evenly spaced between $R_{\mathrm{Ca-C}} = 2.6$ to 5.4 Å. All BME simulations used the same CSVR thermostat parameters as the OPES simulations, with a 0.25 fs timestep and a hydrogen mass of 1 amu (because the mass cannot be set to 2 amu in CP2K to run these simulations, using a shorter timestep compensates for having to use the smaller mass). The free energy was then obtained from integrating the average constraint force according to

$$F(s) = \int_{s_0}^{s} ds\, \langle \lambda(s) \rangle - \frac{2}{\beta}\ln(s) \tag{S2}$$

where $\langle \lambda(s) \rangle$ is the statistical average of the Lagrange multiplier in the SHAKE algorithm[8] and the second term in Eq. (S2) is the entropy contribution from the Jacobi factor.

In Fig. S2, we compare the FES obtained from both the OPES and BME approaches. The two methods agree well, indicating that the ion-pairing FES is insensitive to the choice of enhanced sampling techniques. Nevertheless, both OPES and BME require relatively long sampling times to achieve convergence, which may help explain the discrepancies observed in some earlier AIMD-based studies.

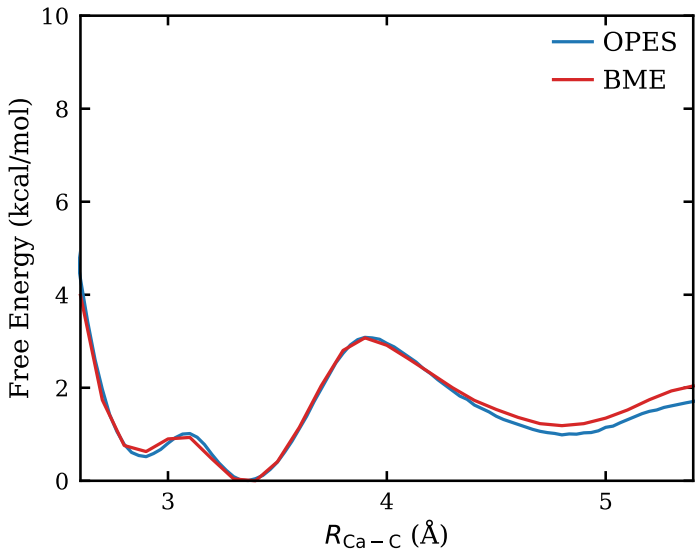

Figure S3 Free-energy surfaces computed using the BME and OPES enhanced-sampling methods. The two methods show excellent agreement.

3. Temperature Effects

Here we report the FES computed using the baseline DFT-revPBE-D3(BJ) MLIP model at different temperatures. As shown in Fig. S4, the temperature dependence in the bidentate and monodentate CIP regions is small, reflecting that the strong cation-ligand binding dominates the energetics in these configurations. In contrast, at the SSIP region and beyond, temperature effects become larger due to the increasing importance of entropy of the water configurations near and shared between the ion pair. Overall, the temperature dependence of the FES remains relatively small in the 300-330 K range. Looking forward, it will be interesting to explore the temperature dependence of the FES at higher temperatures using chemically accurate ECW-TL MLIP models to fully assess the role of entropic contributions.

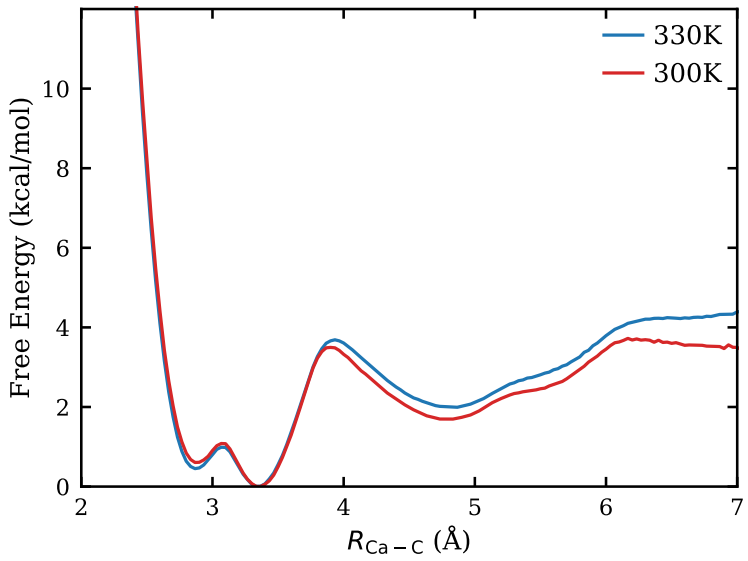

Figure S4 Free-energy surfaces computed at two temperatures with the DFT-revPBE-D3(BJ) MLIP model. The profiles show a relatively small temperature dependence at or near room-temperature.

4. Details and Convergence Tests for Periodic ECW Calculations

For the embedding potential generation, a 216 × 216 × 216 real-space grid is used for the fast Fourier transform (FFT) in the plane-wave DFT calculation, and the parameter F_{Corr} that controls the region of derivative corrections is set to 0.70. Within the projector augmented-wave (PAW) density functional embedding theory (DFET) method, the derivative correction is only evaluated for points within $F_{\mathrm{Corr}}R_{\mathrm{aug}}$, where R_{aug} is the core radius.[9] The embedding potential V_{emb} is optimized by maximizing the extended Wu-Yang functional to a gradient threshold of 10^{-5}. Once the embedding potential is optimized, we project it onto a Gaussian-type orbital (GTO) basis using the EmbeddingIntegralGenerator code[10] to perform ECW calculation:

$$V_{\mu\nu}^{\mathrm{emb}} = \langle \mu | \hat{V}_{\mathrm{emb}} | \nu \rangle \tag{S3}$$

where $V_{\mu\nu}^{\mathrm{emb}}$ represents the one-electron embedding potential integral between atomic orbitals μ and ν. The ECW Hamiltonian can be expressed as

$$\hat{H}_{\mathrm{ECW}} = \hat{H}_{\mathrm{CW}} + \hat{V}_{\mathrm{emb}}. \tag{S4}$$

where $\hat{H}_{\mathrm{CW}}$ is the corresponding correlated wavefunction Hamiltonian of the cluster.

One issue with the current cell and cluster size is that the cluster sits too close to its periodic images. Although the embedding potential correctly accounts for interactions between the cluster and the environment - including all periodic replicas of the environment - it does not include the interactions between the cluster itself and its periodic images. To eliminate this artifact, we therefore used periodic GTO-based methods for the embedded DFT and ECW calculations with the ECW Hamiltonian defined in Eq. (S4), ensuring that the interactions between the cluster and both the periodic environment and cluster images are correctly included. We note this is the first time that the ECW framework has included these periodic images. Largely, the ECW method has been used to study metallic systems, which screen interactions rapidly, such that there was no need to include periodic images of the embedded clusters. But in lower dielectric constant condensed matter, it is fortunate that periodic CW methods and codes now can be utilized with ECW to properly account for all periodic interactions.

In PySCF,[11] the cell precision parameter controls the accuracy of periodic GTO integrals by setting the FFT grid, kinetic-energy cutoff, and lattice-summation cutoff. Figure S5 shows the convergence of SCF energies of periodic GTO DFT calculations with respect to the precision parameter. A precision value of 10^{-10} was used in this work, which yields convergence to better than approximately 0.001 kcal/mol or 1.6×10^{-6} Hartree.

For all periodic GTO calculations in this work, we used a large cc-pVTZ[12] basis set and a def2-TZVPP auxiliary basis[13] for density fitting to accelerate computations. We used a Gaussian smearing of 0.1 eV to stabilize SCF convergence and the SCF energies were converged to a threshold to 10^{-8} Hartree.

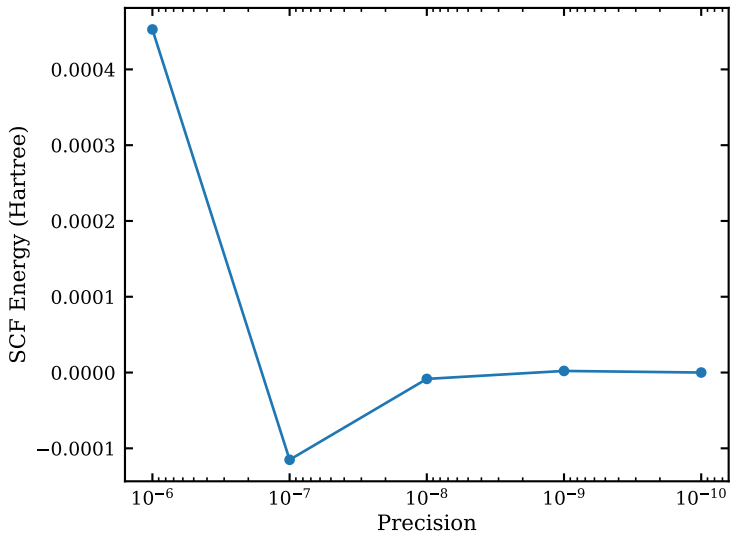

Figure S5 SCF energies as a function of the precision parameter in periodic GTO DFT calculations. A precision parameter of 10^{-10} provides good convergence. The energy zero is defined as the SCF energy calculated at 10^{-10}.

The embedded periodic GTO method was validated against the embedded periodic planewave (PW) method at the DFT-SCAN level (with periodic PW DFT-revPBE-D3(BJ) as the low-level theory for the total system). In Fig. S6, we present an energy parity plot comparing embedded periodic GTO DFT-SCAN and embedded periodic PW DFT-SCAN energies for the dataset used in the first fine-tuning iteration described in the main text (~700 configurations). The two methods agree quite well, considering these are total absolute energies (the error will be far less for actual energy observables, which are energy differences).

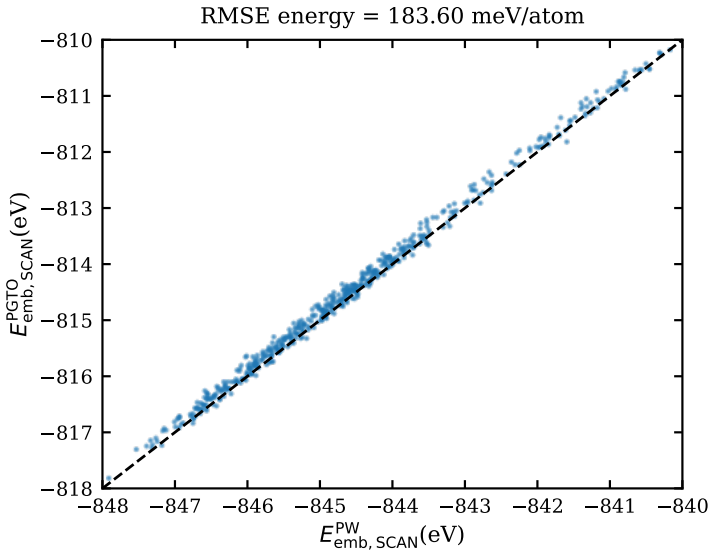

Figure S6 Comparison between embedded periodic GTO DFT-SCAN and embedded periodic PW DFT-SCAN energies, showing satisfactory agreement in total energies.

For the embedded periodic GTO MP2 and LNO-CCSD(T) calculations, after achieving convergence at the periodic Hartree-Fock level, we froze the inner-core 1s orbitals of C and O, and the 1s, 2s, and 2p orbitals of Ca for the later correlated calculations. For the embedded periodic LNO-CCSD(T) calculations,[14] first the canonical HF orbitals were localized using the Pipek-Mezey localization[15] to generate local orbitals and define fragments. The local subspace was defined by freezing occupied and virtual natural orbitals with eigenvalues below user-defined thresholds η_{occ} (η_{vir}) for each local fragments. The periodic LNO-CCSD(T) calculation then was carried out in the resulting truncated orbital space.[14] Note that at the $\eta_{\mathrm{occ}} = \eta_{\mathrm{vir}} = 0$ limit, LNO-CCSD(T) reduces to canonical CCSD(T). Here we fix the ratio $\eta_{\mathrm{occ}}/\eta_{\mathrm{vir}} = 10$ as recommended for molecular LNO-CC[16] and scan η_{vir} to analyze the convergence behavior.

The final embedded periodic LNO-CCSD(T) energies as a function of η_{vir} are plotted in Fig. S6.

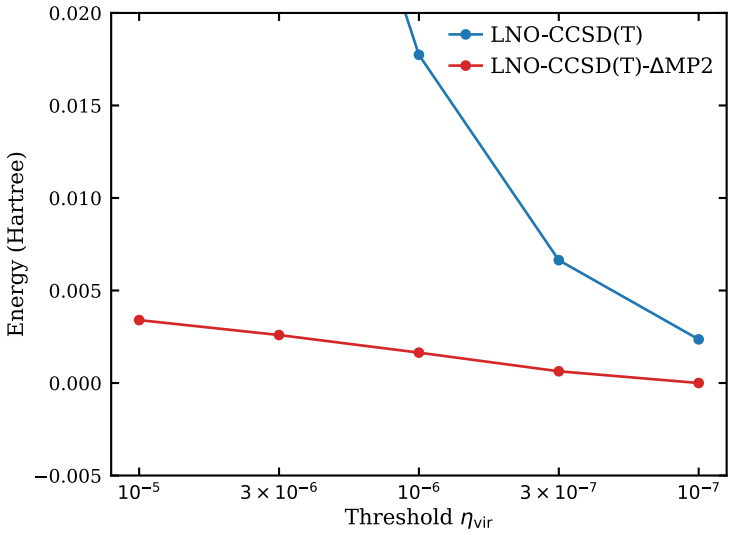

Figure S7 Embedded periodic LNO-CCSD(T) and periodic LNO-CCSD(T)-ΔMP2 energies as function of active space threshold η_{vir}. The energy zero is defined as the LNO-CCSD(T)- ΔMP2 energy calculated at $\eta_{\mathrm{vir}} = 10^{-7}$.

Although the direct LNO-CCSD(T) converges slowly with respect to the virtual space threshold, the MP2-corrected LNO-CCSD(T)-ΔMP2 defined as:

$$E_{\mathrm{LNO-CCSD(T)-\Delta MP2}} = E_{\mathrm{LNO-CCSD(T)}} + (E_{\mathrm{MP2}} - E_{\mathrm{LNO-MP2}}) \tag{S5}$$

converges to within 1 kcal/mol (or 1.6×10^{-3} Hartree) at $\eta_{\mathrm{vir}} = 10^{-6}$. Here, the MP2 correction term in parentheses in Eq. S5 represents the energy difference between periodic MP2 and periodic LNO-MP2. We therefore set $\eta_{\mathrm{vir}} = 10^{-6}$ as a compromise between computational cost and accuracy and use $E_{\mathrm{LNO-CCSD(T)-\Delta MP2}}$ as our reference energy in ECW-TL training.

5. Comparison Between ECW-TL and Direct Cluster Δ-Learning

Finally, we demonstrate the power of our ECW-TL framework by comparing it to the traditional Δ-learning approach. For the direct cluster Δ-learning approach, the high-level reference energy used to finetune baseline MLIP is defined as

$$E_{\Delta-\text{learning}} = E_{\text{baseline}} + \left(E^{\text{cluster}}_{\text{high-level}} - E^{\text{cluster}}_{\text{baseline}}\right) \quad \text{(S6)}$$

where the correction is constructed from an isolated cluster. The key difference between this Δ-learning approach and our ECW-TL framework is that it neglects all interactions between the selected cluster and the surrounding environment. We used the same configurations as in the transfer learning of our embedded-DFT-SCAN model in the main text, but with reference energies redefined according to Eq. (S6) to finetune the baseline DFT-revPBE-D3(BJ) model.

In Fig. S7, we plot the FES computed from both the embedded DFT-SCAN model and the direct cluster Δ-learning approach. Our embedded model clearly is more accurate than the isolated cluster model under the same transfer-learning setup. This result highlights the importance of properly accounting for system-environment interactions when fine-tuning MLIP models.

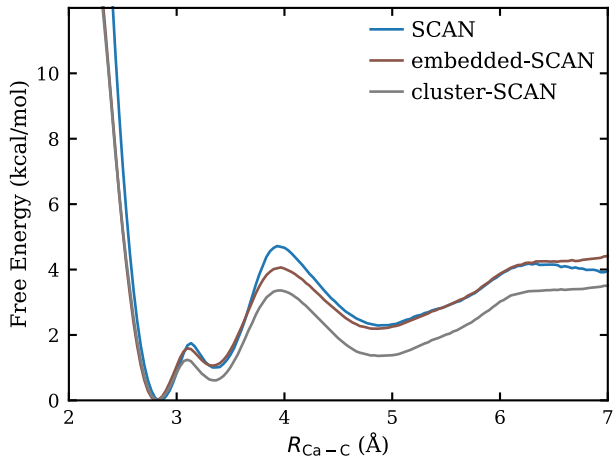

Figure S8 Free-energy surfaces computed from the two transfer-learning DFT-SCAN models compared with the DFT-SCAN reference model.

6. Comparison of DFT-based FESs with previous related studies

The FESs computed from our DFT-revPBE-D3(BJ) and DFT-SCAN models are compared in Fig. S9 with previous studies by Boyn et al.[17] and Piaggi et al. [18] . We find that the DFT-revPBE-D3(BJ)-MLIP-MD results in this work are in *qualitative* agreement with the DFT-revPBE-D3(BJ)-MD results of Boyn et al. in the bidentate and monodentate CIP regions. However, the DFT-MD results in Ref. 17 predict a significantly lower minimum in the SSHIP region, in disagreement with our results. These differences likely arise from limited sampling possible in the previous DFT-MD simulations, where each constrained MD trajectory was sampled for only 10 ps, which may not have been sufficient to achieve full convergence. This comparison highlights the advantage of MLIP-based simulations in obtaining well-converged FESs for ion-pairing systems.

For the MLIP-DFT-SCAN-based results, the model in this work and that of Ref. 18 again agree qualitatively. The remaining quantitative differences may arise from several factors. First, Piaggi et al. employed norm-conserving pseudopotentials, whereas we use all-electron, frozen-core PAW potentials. Second, their simulations were performed in the NPT ensemble, while ours are conducted in the NVT ensemble. Third, the model of Piaggi et al. was trained on a broader set of configurations spanning multiple processes, which may compromise accuracy for ion pairing compared to our model specifically trained for this system.

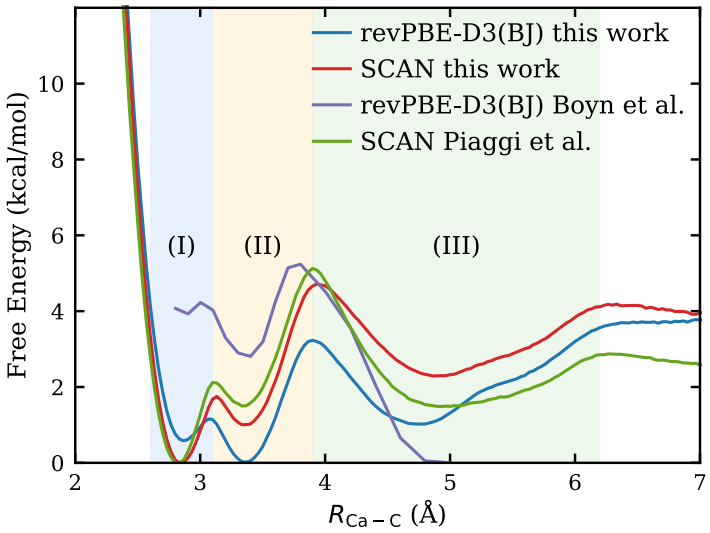

Figure S9 Free-energy surfaces computed from our two DFT-MLIP models compared with previous studies in Refs. 17 (revPBE-D3(BJ)-MD only) and 18 (SCAN-MLIP-MD only).

References

(1) Invernizzi, M.; Parrinello, M. Exploration vs Convergence Speed in Adaptive-Bias Enhanced Sampling. *J. Chem. Theory Comput.* **2022**, *18* (6), 3988–3996. https://doi.org/10.1021/acs.jctc.2c00152.

(2) Thompson, A. P.; Aktulga, H. M.; Berger, R.; Bolintineanu, D. S.; Brown, W. M.; Crozier, P. S.; in 't Veld, P. J.; Kohlmeyer, A.; Moore, S. G.; Nguyen, T. D.; Shan, R.; Stevens, M. J.; Tranchida, J.; Trott, C.; Plimpton, S. J. LAMMPS - a Flexible Simulation Tool for Particle-Based Materials Modeling at the Atomic, Meso, and Continuum Scales. *Comput. Phys. Commun.* **2022**, *271*, 108171. https://doi.org/10.1016/j.cpc.2021.108171.

(3) Tribello, G. A.; Bonomi, M.; Branduardi, D.; Camilloni, C.; Bussi, G. PLUMED 2: New Feathers for an Old Bird. *Comput. Phys. Commun.* **2014**, *185* (2), 604–613. https://doi.org/10.1016/j.cpc.2013.09.018.

(4) Bussi, G.; Donadio, D.; Parrinello, M. Canonical Sampling through Velocity Rescaling. *J. Chem. Phys.* **2007**, *126* (1), 014101. https://doi.org/10.1063/1.2408420.

(5) Carter, E. A.; Ciccotti, G.; Hynes, J. T.; Kapral, R. Constrained Reaction Coordinate Dynamics for the Simulation of Rare Events. *Chem. Phys. Lett.* **1989**, *156* (5), 472–477. https://doi.org/10.1016/S0009-2614(89)87314-2.

(6) DEN OTTER, W. K.; BRIELS, W. J. Free Energy from Molecular Dynamics with Multiple Constraints. *Mol. Phys.* **2000**, *98* (12), 773–781. https://doi.org/10.1080/00268970009483348.

(7) Kühne, T. D.; Iannuzzi, M.; Del Ben, M.; Rybkin, V. V.; Seewald, P.; Stein, F.; Laino, T.; Khaliullin, R. Z.; Schütt, O.; Schiffmann, F.; Golze, D.; Wilhelm, J.; Chulkov, S.; Bani-Hashemian, M. H.; Weber, V.; Borštnik, U.; Taillefumier, M.; Jakobovits, A. S.; Lazzaro, A.; Pabst, H.; Müller, T.; Schade, R.; Guidon, M.; Andermatt, S.; Holmberg, N.; Schenter, G. K.; Hehn, A.; Bussy, A.; Belleflamme, F.; Tabacchi, G.; Glöß, A.; Lass, M.; Bethune, I.; Mundy, C. J.; Plessl, C.; Watkins, M.; VandeVondele, J.; Krack, M.; Hutter, J. CP2K: An Electronic Structure and Molecular Dynamics Software Package - Quickstep: Efficient and Accurate Electronic Structure Calculations. *J. Chem. Phys.* **2020**, *152* (19), 194103. https://doi.org/10.1063/5.0007045.

(8) Ryckaert, J.-P.; Ciccotti, G.; Berendsen, H. J. C. Numerical Integration of the Cartesian Equations of Motion of a System with Constraints: Molecular Dynamics of *n*-Alkanes. *J. Comput. Phys.* **1977**, *23* (3), 327–341. https://doi.org/10.1016/0021-9991(77)90098-5.

(9) Yu, K.; Libisch, F.; Carter, E. A. Implementation of Density Functional Embedding Theory within the Projector-Augmented-Wave Method and Applications to Semiconductor Defect States. *J. Chem. Phys.* **2015**, *143* (10), 102806. https://doi.org/10.1063/1.4922260.

(10) Krauter, C. M.; Carter, E. A. EmbeddingIntegralGenerator. https://github.com/EACcodes/EmbeddingIntegralGenerator.

(11) Sun, Q.; Zhang, X.; Banerjee, S.; Bao, P.; Barbry, M.; Blunt, N. S.; Bogdanov, N. A.; Booth, G. H.; Chen, J.; Cui, Z.-H.; Eriksen, J. J.; Gao, Y.; Guo, S.; Hermann, J.; Hermes, M. R.; Koh, K.; Koval, P.; Lehtola, S.; Li, Z.; Liu, J.; Mardirossian, N.; McClain, J. D.; Motta, M.; Mussard, B.; Pham, H. Q.; Pulkin, A.; Purwanto, W.; Robinson, P. J.; Ronca, E.; Sayfutyarova, E. R.; Scheurer, M.; Schurkus, H. F.; Smith, J. E. T.; Sun, C.; Sun, S.-N.; Upadhyay, S.; Wagner, L. K.; Wang, X.; White, A.; Whitfield, J. D.; Williamson, M. J.; Wouters, S.; Yang, J.; Yu, J. M.; Zhu, T.; Berkelbach, T. C.; Sharma, S.; Sokolov, A. Yu.; Chan, G. K.-L. Recent Developments

in the PySCF Program Package. *J. Chem. Phys.* **2020**, *153* (2), 024109. https://doi.org/10.1063/5.0006074.
(12) Dunning, T. H. Gaussian Basis Sets for Use in Correlated Molecular Calculations. I. The Atoms Boron through Neon and Hydrogen. *J. Chem. Phys.* **1989**, *90* (2), 1007–1023. https://doi.org/10.1063/1.456153.
(13) Weigend, F.; Ahlrichs, R. Balanced Basis Sets of Split Valence, Triple Zeta Valence and Quadruple Zeta Valence Quality for H to Rn: Design and Assessment of Accuracy. *Phys. Chem. Chem. Phys.* **2005**, *7* (18), 3297–3305. https://doi.org/10.1039/B508541A.
(14) Ye, H.-Z.; Berkelbach, T. C. Periodic Local Coupled-Cluster Theory for Insulators and Metals. *J. Chem. Theory Comput.* **2024**, *20* (20), 8948–8959. https://doi.org/10.1021/acs.jctc.4c00936.
(15) Pipek, J.; Mezey, P. G. A Fast Intrinsic Localization Procedure Applicable for Ab Initio and Semiempirical Linear Combination of Atomic Orbital Wave Functions. *J. Chem. Phys.* **1989**, *90* (9), 4916–4926. https://doi.org/10.1063/1.456588.
(16) Rolik, Z.; Szegedy, L.; Ladjánszki, I.; Ladóczki, B.; Kállay, M. An Efficient Linear-Scaling CCSD(T) Method Based on Local Natural Orbitals. *J. Chem. Phys.* **2013**, *139* (9), 094105. https://doi.org/10.1063/1.4819401.
(17) Boyn, J.-N.; Carter, E. A. Characterizing the Mechanisms of Ca and Mg Carbonate Ion-Pair Formation with Multi-Level Molecular Dynamics/Quantum Mechanics Simulations. *J. Phys. Chem. B* **2023**, *127* (50), 10824–10832. https://doi.org/10.1021/acs.jpcb.3c05369.
(18) Piaggi, P. M.; Gale, J. D.; Raiteri, P. Ab Initio Machine-Learning Simulation of Calcium Carbonate from Aqueous Solutions to the Solid State. *Proc. Natl. Acad. Sci.* **2025**, *122* (41), e2415663122. https://doi.org/10.1073/pnas.2415663122.